

# **Modeling ice-shelf cavities using Lagrangian elements**

A.A. Stern,<sup>1</sup>, A. Adcroft<sup>1</sup> and O. Sergienko<sup>1</sup>, G. Marques<sup>1</sup>, R. Hallberg<sup>1</sup>

2      **Key Points:**

3

- 4      • A novel modeling framework is developed to model breakable ice shelves and ice-shelf cavities  
5      using Lagrangian elements, held together by numerical bonds.
- 6      • The ocean circulation beneath a (static) Lagrangian ice shelf is almost indistinguishable  
7      from the circulation beneath an Eulerian ice-shelf model run in an identical configuration, which  
8      provides a proof of concept for the Lagrangian model.
- 9      • Enhanced ocean mixing occurs near the ice front after a large calving event, which warms  
10     the ocean surface and cools the water column at depth. The cool sub-surface anomalies enter  
11     the ice shelf cavity and cause reduced basal melt in the period following the calving event.

---

A. A. Stern, Geophysical Fluid Dynamics Laboratory, Princeton University

A. Adcroft, Geophysical Fluid Dynamics Laboratory, Princeton University

O. Sergienko, Geophysical Fluid Dynamics Laboratory, Princeton University

G. Marques, Geophysical Fluid Dynamics Laboratory, Princeton University

R. Hallberg, Geophysical Fluid Dynamics Laboratory, Princeton University

**12 Abstract.** The current generation of ice-ocean models is unable to rep-  
13 resent ice-shelf calving in a physically realistic way, despite the controlling  
14 role that calving plays in the setting mass balance and extent of Antarctic  
15 ice shelves. The infrequency of large calving events together with the diffi-  
16 culty of placing observational instruments around tabular icebergs means that  
17 little is known about how calving icebergs affect the ocean. In this study we  
18 present a novel model of an ice-shelf cavity below a breakable ice shelf con-  
19 structed of Lagrangian elements. We validate the Lagrangian ice shelf model  
20 by simulating the flow beneath a (static) idealized ice shelf, and comparing  
21 the results to an Eulerian model simulations with identical configuration. The  
22 Lagrangian model is then used to simulate the ocean's response to a tabu-  
23 lar iceberg calving away from the ice shelf. The results show a calving ice-  
24 berg can lead to large changes in the surrounding ocean. Changes in circu-  
25 lation patterns and enhanced vertical mixing are observed at the ice front  
26 and around the iceberg following the calving event. The vertical mixing at  
27 the ice front warms the ocean surface and cools the water column at depth,  
28 allowing cooler waters to enter the ice shelf cavity, which in turn leads to re-  
29 duced melt rates within the cavity. A Taylor column is observed below the  
30 iceberg, which moves with the iceberg as it drifts into the open ocean. As  
31 the tabular iceberg drifts further from the ice shelf, the circulation within  
32 the ice shelf cavity tends towards a new steady state, consistent with the new  
33 ice shelf geometry.

## 1. Introduction

34 Satellite observations show that ice-shelf decay occurs via two main processes: melting  
35 and breaking [Depoorter et al , 2013; Rignot et al , 2013]. Each of these is responsible  
36 for approximately half of the ice-shelf decay, and each influences the surrounding ocean  
37 (and ice-shelf geometry) in a distinct way. Melting at the base of ice shelves causes fluxes  
38 of freshwater into the ice-shelf cavity. The input of buoyant meltwater creates rising density  
39 plumes, which are guided along the ice-shelf base, and help drive ocean circulation beneath  
40 the ice shelves [MacAyeal , 1984; Holland and Feltham , 2006]. Over time, melting at the  
41 ice-shelf base can erode the ice shelf, gradually altering the ice-shelf geometry. In contrast,  
42 iceberg calving causes sudden changes to the ice-shelf geometry, and releases giant icebergs  
43 into the ocean. After calving, these tabular icebergs can travel large distances and impact  
44 ocean hydrography [Martin and Adcroft , 2010; Stern et al , 2015], sea-ice formation  
45 [Robinson and Williams , 2012; Stern et al , 2016] and ocean biology [Smith et al , 2007;  
46 Vernet et al , 2012; Biddle et al , 2015] many miles away.

47 Modeling the ocean beneath the ice shelves presents a unique set of challenges, since  
48 (i) the presence of ice shelves provides a quasi-rigid upper boundary for the ocean model  
49 which is not encountered elsewhere in the ocean, and (ii) melting and breaking ice shelves  
50 imply changing ocean boundary conditions which present numerous numerical difficulties.

51 The earliest models of ocean ice-shelf cavities were developed using static ice shelves  
52 with a fixed shape [Hellmer and Olbers , 1989; Determan and Gerdes , 1994; Grosfeld et  
53 al , 1997; Holland and Jenkins , 2001; Losch , 2008]. In these models, ice-shelf melting  
54 was represented through salinity and temperature fluxes, while the ice-shelf geometry

55 remained unchanged. Later models of ice-shelf cavities allowed the ice-shelf geometry  
56 to evolve as the ice shelf melted, permitting the study of coupled ocean-ice phenomena  
57 [Gladish et al , 2012; Sergienko , 2013]. More recently, dynamic ice-shelf models have  
58 been coupled to the ocean cavity, allowing the study of grounding line migration which is  
59 of key importance for sea level rise projections [Grosfeld and Sandhger , 2004; Goldberg  
60 et al , 2012; De Rydt and Gudmundsson , 2016; Seroussi et al , 2017].

61 All models of ice-shelf cavities to date have omitted ice-shelf breaking and iceberg  
62 detachment. This is because (i) there is much uncertainty about the physics that govern  
63 ice-shelf breaking [Benn et all , 2007; Alley et al , 2008; Levermann et al , 2012; Bassis  
64 and Jacobs , 2013], and (ii) current models of ice-shelf cavities represent the ice shelves on  
65 static Eulerian grids, which do not lend themselves to modeling iceberg detachment and  
66 drift. In contrast, existing *iceberg* models represent icebergs as Lagrangian particles, since  
67 this is a convenient way to model discrete objects traveling over large distances [Bigg et  
68 al , 1997; Gladstone et al , 2001; Martin and Adcroft , 2010; Marsh et al , 2015]. To date  
69 there has been no real effort to synthesize these two approaches (i.e.: to combine ice shelf  
70 and iceberg models).

71 In this study we develop a new ice-shelf cavity model where the ice shelf is simulated  
72 with Lagrangian elements [Stern et al , 2017]. In this model, the ice shelf is constructed  
73 out of Lagrangian elements which are bonded together by numerical bonds (see schematic  
74 Figures 1). This Lagrangian framework allows for large pieces of the ice shelf to break away  
75 and become tabular icebergs. An example of this enhanced capability of the Lagrangian  
76 model is demonstrated in Figures 2, which shows a tabular iceberg drifting away from an  
77 idealized ice shelf.

78 The goals of this study are (i) to introduce and describe the Lagrangian ice-shelf model,  
79 (ii) to validate the Lagrangian model by simulating the flow beneath a static idealized  
80 ice shelf cavity, and comparing it to an Eulerian ice-shelf model run in an identical con-  
81 figuration, and (iii) to demonstrate the enhanced capabilities of the Lagrangian ice-shelf  
82 model by simulating a large iceberg calving away from the idealized ice shelf. Modeling  
83 the ocean during and after a calving event, allows us to observe how the calving event  
84 affects the ocean near and beneath the ice shelf, and how changes in the ocean feedback  
85 onto the ice shelf.

## 2. Lagrangian model description

86 The Kinematic Iceberg Dynamics (KID) model is a Lagrangian model that has been  
87 developed in order to simulate ice-shelf cavities with breakable ice shelves. The model  
88 represents ice shelves using Lagrangian elements joined together by numerical bonds. By  
89 breaking these bonds, the model is able to simulate ice-shelf calving and iceberg breakup.

90 In this section we describe the Lagrangian ice-shelf model. A more complete description  
91 of the model including numerical methods and algorithms used to track the numerical  
92 bonds can be found in Stern et al [2017].

### 2.1. Kinematic Iceberg Dynamics model

93 The KID model is a Lagrangian particle-based model, in that the objects of the model  
94 are Lagrangian elements. Each Lagrangian element represents a column of ice that is  
95 floating in the ocean. The elements have their own position, velocity, mass, and a set  
96 of dimensions, which can evolve in time. Each element moves according to its own mo-  
97 mentum balance which is computed in the (Lagrangian) reference frame of the element.

98 The elements experience oceanic, sea ice and atmospheric drag forces, as well as a forces  
 99 due to sea surface height gradients, and the Coriolis force [Bigg et al , 1997; Gladstone  
 100 et al , 2001; Martin and Adcroft , 2010; Stern et al , 2017]. The elements also interact  
 101 with other elements and can be ‘bonded’ together by numerical bonds, which allow many  
 102 elements to move together as a unit. By bonding many ice elements together, the model  
 103 is able to form larger structures, such as tabular icebergs or ice shelves (Figure 1).

## 2.2. Equations of motion

The momentum equation for each element is given by

$$M \frac{D\vec{u}}{Dt} = \vec{F}_A + \vec{F}_W + \vec{F}_R + \vec{F}_C + \vec{F}_{SS} + \vec{F}_{SI} + \vec{F}_{IA}, \quad (1)$$

104 where  $\frac{D}{Dt}$  is the total (Lagrangian) derivative,  $M$  is the mass of the element,  $\vec{u}$  is the  
 105 velocity of the element, and the terms on the right hand side give the forces on the  
 106 element due to air drag ( $\vec{F}_A$ ), water drag ( $\vec{F}_W$ ), sea-ice drag ( $\vec{F}_{SI}$ ), Coriolis force ( $\vec{F}_C$ ),  
 107 wave radiation force ( $\vec{F}_R$ ), sea surface slope ( $\vec{F}_{SS}$ ), and interactions with other elements  
 108 ( $\vec{F}_{IA}$ ).

109 The forces on each element are set up such that in the absence of interactive forces,  
 110 the ice elements follow the same equations used in iceberg drift models [Bigg et al , 1997;  
 111 Gladstone et al , 2001; Martin and Adcroft , 2010]). This ensures that when an element  
 112 breaks away from an ice shelf and drifts in the open ocean, it is modeled as a freely drifting  
 113 iceberg. When an element is connected to the ice shelf (or larger ice structure), it also  
 114 experiences forces due to interactions with the elements around it. The details of these  
 115 interactive forces between elements are described below. A complete description of the  
 116 other forces acting on the iceberg is provided in Stern et al [2017].

### 2.3. Interactive Forces

Interactive forces are applied between elements to prevent elements overlapping with neighboring elements, and prevent ‘bonded’ elements from moving apart from one another (see Figures 1a). The interactive forces are modeled as damped elastic forces: For two elements  $i$  and  $j$  at positions  $\vec{x}_i$  and  $\vec{x}_j$ , the elastic and damped components of the interactive force are given by

$$(\vec{F}_e)_{ij} = -\kappa_e \left( d_{ij} - L_{ij} \right) M_{ij} \vec{r}_{ij}, \quad (2)$$

and

$$(\vec{F}_d)_{ij} = -M_{ij} c_{r_{||}} P_{\vec{r}_{ij}} \cdot (\vec{u}_i - \vec{u}_j), \quad (3)$$

respectively. Here  $d_{ij} = |\vec{x}_i - \vec{x}_j|$  is the distance between the elements,  $\vec{r}_{ij} = \frac{(\vec{x}_i - \vec{x}_j)}{|\vec{x}_i - \vec{x}_j|}$  is the directional unit vector between element.  $L_{ij}$  is the average diameter of the two elements (assuming a circular shape for the elements),  $\kappa_e$  is the spring constant, and  $M_{ij}$  is the minimum of the masses of elements  $i$  and  $j$ .  $P_{\vec{r}_{ij}}$  is the projection matrix that projects onto  $\vec{r}_{ij}$ , and  $c_{r_{||}}$  is the drag coefficient. We set  $c_{r_{||}} = 2\sqrt{\kappa_e}$ , so that the elastic force is critically damped. The total interactive  $\vec{F}_{IA}$  on an element is found by summing up the all the interactive forces with other elements.

### 2.4. Melt rates

The thickness and extent of the Lagrangian elements change due to melting when they are exposed to above-freezing ocean mixed-layer temperatures. The melt rates of the elements in the interior of a large structure (such as an ice shelf or large icebergs) are parametrized using the three-equation model, which is a typically melt rate parametrization used to model basal melt beneath ice shelves [Holland and Jenkins, 1999]. The melt

129 rates of freely floating ice elements (not bonded to other elements) are parametrized using  
130 standard parametrizations for iceberg [Bigg et al , 1997; Gladstone et al , 2001; Martin  
131 and Adcroft , 2010]. For elements at the edge of large structures (with edges partly ex-  
132 poses to the open ocean) the melt rates are computed using a weighted sum of the ice  
133 shelf and and iceberg melt rate parametrization, with the weights being proportional to  
134 the fraction of the element's perimeter which exposed to the open ocean [Stern et al ,  
135 2017].

## 2.5. Initializing element geometry and packing

136 The elements in the Lagrangian model are shaped as equally-sized regular hexagons (al-  
137 though they are treated as circular for the purpose of element interactions). We initialize  
138 the Lagrangian model by positioning the elements in a staggered lattice of equally-size  
139 hexagons, so that the elements fit together and perfectly tile the ice-shelf surface (Figures  
140 1). Hexagonal elements are used so that when adjacent pairs of elements are bonded to-  
141 gether, the network of bonds form equilateral triangles, which gives rigidity to the larger  
142 structure [Stern et al , 2017]. By using hexagonal elements, which can be packed to-  
143 gether without any gaps, the element initialization is perfectly space filling. This allows  
144 the model to simulate continuous ice shelves (without gaps or crevasses), and allows the  
145 results to be more easily comparable with Eulerian ice shelf models. In this study, we  
146 only use hexagonal elements, however, other element geometries, can be used when less  
147 precision is needed.

## 2.6. Interpolation and aggregation onto the Lagrangian grid

At every time step, ice-shelf fields are passed from the ice-shelf model to the ocean model and from the ocean model to the ice-shelf model. Fields which are passed from the ocean model to the Lagrangian ice shelf model have to be interpolated from the Eulerian grid onto the Lagrangian grid (i.e.: onto the elements). This is done using a bilinear interpolation scheme. Four ocean fields are passed from the ocean model to the ice-shelf model: temperature, salinity and zonal and meridional velocities.

At the end of an ice-shelf model time step, ice-shelf fields are aggregated from the elements back onto the Eulerian ocean grid, and are then passed from the ice-shelf model to the ocean model. The aggregation from the Lagrangian elements onto the Eulerian grid is done by calculating the fraction of each element's volume that lies in each ocean grid cell, and dividing the fields in proportion to this fraction. For example, the amount of ice mass aggregated onto a given ocean grid cell is found by summing up the masses of all elements which intersect that grid cell, only counting the part of an element's mass that actually intersects the ocean grid cell. When calculating the intersection between an element and a grid cell, we assume that the elements have surface areas that are shaped as regular hexagons. Seven fields are passed from the ice-shelf models to ocean model: iceberg mass and surface area (used the upper-ocean pressure field), temperature flux, salinity flux and mass flux, and meridian and zonal velocity (used to calculate the momentum flux).

### 3. Experiment Setup

#### 3.1. Domain configuration

In order for our simulations to be easily comparable to previous models of ice-shelf cavities, we use an experimental setup based on the configuration created for the Marine Ice Ocean Modeling Inter-comparison Project (MISOMIP) [Asay-Davis et al , 2016]. The configuration consists of an idealized ice shelf in a rectangular domain  $L_x = 80\text{km}$  long and  $L_y = 480\text{km}$  wide. The ice shelf is grounded on the southern side of the domain with the ice-shelf front at  $y=650\text{km}$ . The ice thickness and bottom topography of this setup are shown in Figure 3. The configuration is the same as that of the Ocean0 setup in the MISOMIP, with three changes made:

1. The ‘calving criteria’ used in the MISOMIP study (which states that all points in the ice shelf with thickness less than 100m are set to zero thickness) has not been used.
  2. The ice shelf has been thickened on the flanks of the domain, so that the latitude of the grounding line increases away from the center of the ice shelf.
  3. The ice shelf is configured to be symmetric about its meridional center line ( $x = \frac{L_x}{2}$ ).
- This was achieved by using the average of the left and right flanks of the ice-shelf thickness. These three changes were made in order to make the circulation beneath the ice shelf easier to interpret.

#### 3.2. Ocean Model

The Lagrangian and Eulerian ice shelves are coupled to the MOM6 ocean model [Hallberg et al , 2013]. The ocean model is run using a hybrid vertical coordinate system which blends a sigma-level and a z-level coordinate [Stern et al , 2017], implemented using the ALE method [White et al , 2009]. In this vertical coordinate, model layers bend

underneath surface topography (i.e.: the ice shelf), as they would in a sigma coordinate model, and intersect the bottom topography, as they would in a z-coordinate model. The model has 72 vertical layers and has a horizontal resolution of  $\Delta x = 2$  km. The numerical simulations were all repeated using an isopycnal coordinate (without ALE regridding-remapping). The results were qualitatively similar to the hybrid-coordinate results, and are therefore not presented here.

The ocean parameters used in the simulations are as specified in the MISOMIP configuration [Asay-Davis et al , 2016], and are shown in Table 1. The simulation is initialized from rest, with horizontally uniform initial ocean temperature and salinity profiles which vary linearly between specified open-ocean surface and bottom values:  $T_{top} = -1.9^{\circ}\text{C}$ ,  $T_{bottom} = 1.0^{\circ}\text{C}$ ,  $S_{top} = 33.8$  psu,  $S_{bottom} = 34.7$ . The maximum ocean depth is  $H_{ocean} = 720$  m. A sponge layer is used on the northern boundary, which relaxes back to the initial temperature and salinity with a relaxation time scale of  $T_{sponge} = 0.1$  days over a distance of 10 km. Melting is set to zero for ocean cells where the ocean column thickness is less than 10m.

### 3.3. Initializing Lagrangian elements:

The Lagrangian ice shelf is created using 10882 Lagrangian hexagonal elements with sides of length  $S = 0.98$  km . The positions of the hexagonal elements are initialized by packing them together in a space-filling staggered lattice. Gaps along the boundaries are filled in using smaller elements so that the total ice-shelf area is preserved. The initial mass of the ice elements is determined using bilinear interpolation from a prescribed gridded ice mass field.

### 3.4. Eulerian ice-shelf:

208 We validate the Lagrangian ice shelf model by comparing the results to the results found  
 209 using an Eulerian ice shelf model in an identical static ice shelf configuration (see below).  
 210 The Eulerian ice-shelf simulation is performed using an existing Eulerian ice-shelf cavity  
 211 model [Goldberg et al , 2012], which is an optional module of the the MOM6 ocean model.  
 212 The ice shelf is initialized on the same grid as the ocean model with a horizontal resolution  
 213 of  $\Delta x = 2$  km. The ice-shelf thickness field is initialized using the same ice-shelf draft used  
 214 for the Lagrangian model (Figure 3). The melt rates in the Eulerian ice-shelf simulation  
 215 are calculated using the 3 equation model for ice-shelf decay [Holland and Jenkins, 1999],  
 216 with the same parameters used to calculate the ice shelf melt rates in the Lagrangian  
 217 model.

### 3.5. Static ice shelf simulation:

218 We test the Lagrangian ice shelf model by simulating the flow beneath the idealized  
 219 ice shelf with the ice shelf being held statice (i.e.: elements are held stationary). In this  
 220 simulation the ice shelf is thermodynamically active and is able to ‘melt’ but has a time-  
 221 invariant thickness (as specified in the Ocean0 experiment in the MISOMIP [Asay-Davis  
 222 et al , 2016]). In this setup, ice-shelf melting generates temperature and salinity fluxes into  
 223 the ocean, but does not change the thickness of the ice shelf / ice elements. A constant  
 224 wind stress  $\vec{\tau} = \langle \tau_x, \tau_y \rangle = \langle 0.05, 0.05 \rangle \frac{N}{m^2}$  is applied to the ocean surface. Note that  
 225 this wind stress is was not applied in the original MISOMIP experiments [Asay-Davis et  
 226 al , 2016]. The model is spun up for 5 years, and the analysis is done on the second 5  
 227 years after the spinup.

### 3.6. Iceberg calving simulation:

In a second experiment, the Lagrangian ice shelf model is used to simulate a tabular iceberg detaching from the ice shelf, and drifting into the open ocean. The iceberg calving simulation is initialized using the final state of the static Lagrangian ice shelf simulation (i.e.: at time  $t = 10$  years). When initializing the calving event, we bypass the question of how to prescribe a physical calving law [Benn et all , 2007; Alley et al , 2008; Levermann et al , 2012; Bassis and Jacobs , 2013] by manually breaking off a semi-circular iceberg.

In the iceberg calving simulation, all ice elements initially within a 14.4 km radius of the center of the ice front to move freely while the other ice elements continue to be held stationary. Ice elements less than 12 km from the center of the ice front, are bonded together to form a semi-circular tabular iceberg. A ring of elements whose distance,  $d$ , from the ice front center obeys  $12 \text{ km} \leq d \leq 14.4 \text{ km}$ , are allowed to move freely, but have all their bonds removed. Elements in this half annulus represent fragments of the ice shelf which calve into small pieces during the calving event.

**Should these two simulations be included?**

#### 3.6.1. Fixed iceberg velocity simulation

To aid in the analysis of the ocean response to iceberg calving, another iceberg calving simulation was preformed, using a fixed iceberg velocity. This fixed velocity iceberg simulation is identical to the iceberg calving simulation (Section 3.6), except that the velocity of the calving icebergs is prescribed as  $\vec{v} == < 0, 0.01 >$  m/s. Since the iceberg speed is prescribed, this simulation is not fully coupled.

#### 3.6.2. Missing-Iceberg simulation

249 A simulation is preformed to help analyze how the changing ice shelf geometry affects  
250 the sub-ice-shelf circulation and hydrography. In this simulation, calving iceberg (with the  
251 same geometry as the iceberg simulations above) is removed at the start of the simulation,  
252 and the simulation is spun up from rest. The simulation is run for 10 years, so that it is  
253 easily comparable to the Static ice shelf simulation (described in Section 3.5).

## 4. Static ice-shelf simulation results

### 4.1. Static ice-shelf simulation

254 The results in the Lagrangian static ice-shelf simulation fit within the current under-  
255 standing of ice-shelf cavity circulations based on ice-shelf observations [MacAyeal , 1984;  
256 Lewis and Perkin , 1986; Jacobs et al , 2011] and previous modeling efforts [Determan and  
257 Gerdes , 1994; Holland and Feltham , 2006; Losch , 2008]. The ocean temperatures inside  
258 the domain are warmer than the in-situ freezing point (Figure 4a), and cause melting at  
259 the ice-shelf base (Figure 5a). The meltwater entering the domain is more buoyant than  
260 the water around it, and rises along the ice shelf as a cool fresh plume (Figure 4b,c). This  
261 injection of positive buoyancy at depth drives a clockwise circulation outside of the ice-  
262 shelf cavity (Figure 6a), providing the ice-shelf cavity with a continuous supply of warm  
263 water, which provides the thermal energy required for continuous ice-shelf melt. Strong  
264 meridional jets are observed at the ice front along the flanks of the domain, fluxing water  
265 into the ice shelf cavity on the eastern flank and allowing water to leave the ice shelf  
266 cavity on the western side (Figure ??a). The meridional flow in the center of the ice front  
267 is much smaller, consistent with the dynamical barrier at the ice shelf front discussed in  
268 previous modeling and experimental studies [Holland and Jenkins , 2001; Stern et al ,  
269 2014].

270 The highest melt rates are observed within 100km of the grounding line (Figure 5a).  
271 These elevated melt rates are caused by the presence of warm water (Figure 5b) and  
272 increased ocean velocities (Figure 5c) near the grounding line, as well as the fact that  
273 freezing point of ice decreases with increasing pressure. Elevated melt rates are also seen  
274 near the ice front, caused by strong currents running along the ice-shelf front (Figure 5c).

275

#### 4.2. Comparison of Lagrangian and Eulerian ice-shelf models

276 The Lagrangian ice-shelf model results are qualitatively similar to most of the sim-  
277 ulations from the MISOMIP experiment [Asay-Davis et al , 2016], which use a similar  
278 configuration (see Section 3.4). To get a quantitative comparison, we compare the La-  
279 grangian ice-shelf model results to a simulation using an Eulerian ice-shelf model with an  
280 identical configuration. Since the Lagrangian and Eulerian ice shelf models are coupled  
281 to the same ocean model and the ice shelf models use the same parametrization for ice  
282 shelf melt, we expect the results of the two models to be the almost the same, with the  
283 only differences arising from the interpolation and aggregation schemes (see Section 2.6).  
284 This allows us to use the Eulerian ice shelf model to validate the Lagrangian model.

285 The results show that two simulations are almost indistinguishable. This is demon-  
286 strated, for example, in Figures 6, which shows the time-averaged barotropic stream  
287 function of the Lagrangian (Figures 6a) and Eulerian (Figures 6b) simulations, and the  
288 difference between the two (Figures 6c). The difference between the Lagrangian and  
289 Eulerian barotropic stream functions are two orders of magnitude smaller than typical  
290 differences observed between simulations using different models in the MISOMIP [Asay-  
291 Davis et al , 2016]. The similarity of the Lagrangian and Eulerian simulations are also

292 reflected in the fact that the simulations have very similar ice-shelf melt rates and ocean  
293 temperature/salinity profiles (shown in Figures S1 and Figures S2 in the supplementary  
294 materials).

295 The agreement between the Eulerian and Lagrangian simulations is a confirmation that  
296 the Lagrangian model is able to simulate sub-ice-shelf cavities as well as the Eulerian  
297 model does. This is a good starting point for moving beyond the capabilities of the  
298 Eulerian model.

## 5. Iceberg calving simulation results

299 The infrequency of large calving events together with the difficulty of placing observa-  
300 tional instruments around tabular icebergs means that little is known about how calving  
301 icebergs affect ocean circulation around the iceberg and at the ice front. The Lagrangian  
302 ice shelf model developed in this study allows us for the first time to simulate an iceberg  
303 calving away from the ice shelf, and to study what effect this has on the ocean around the  
304 iceberg and beneath the ice shelf. Since the Lagrangian iceberg/ice shelf model is fully  
305 coupled to the ocean, the iceberg motion affects the ocean hydrography, and the changing  
306 ocean conditions feedback onto the ice.

307 The results below show that the calving of a large tabular iceberg can cause significant  
308 changes to the ocean stratification and circulation around the iceberg and at the ice shelf  
309 front. Changing conditions at the ice front alter the temperature fluxes into the ice shelf  
310 cavity, which impacts the hydrography inside the ice shelf cavity, and drives changes to the  
311 ice-shelf melt rates across the entire ice shelf. Local changes to the ocean hydrography are  
312 also observed around the iceberg. A Taylor column is observed below the iceberg, which  
313 travels with the iceberg as it drifts into the open ocean.

### 5.1. At the ice front

After the iceberg calves, the large semi-circular tabular iceberg drifts to the northeast, driven primarily by the wind and Coriolis force. As this large iceberg and the smaller fragments moves through the water a warming of the sea surface temperature is observed around the iceberg and at the ice front (Figure 2). The warm anomalies near the ice front persist and strengthen, even once the large iceberg fragment has drifted away. Part of this warmed surface water at the ice front is advected to west by the strong currents at the ice front (Figure 2c). On the western side of the domain, most of this warm anomaly is advected northwards, while some of the warmth is forced southward, and is able to subduct beneath ice shelf on the western side of the ice shelf front.

In addition to the surface warming, a subsurface cooling is also observed around the iceberg and at the ice front in the days following the calving event (Figure 7). The sub-subsurface cooling and warm surface temperature anomalies are accompanied by a freshening at depth and increase in surface salinity (not shown). Since the background stratification has positive temperature and salinity gradients (cold/fresh water above over warm/salty), the pattern of warm salty surface anomalies above cold fresh subsurface anomalies suggests that these changes are driven by enhanced vertical mixing.

At the ice front, the subsurface negative temperature anomalies strengthen over time and within a month of the calving event, the negative anomalies occupy most of the water column close to the ice front (Figure 8). The zonal current along the ice front drives the cool anomaly to the west, causing an enhancement of the cool anomalies on the western side of the ice shelf front (Figure 8c). Most of the subsurface cooling occurs outside of the ice shelf cavity, as the dynamical barrier caused by the ice shelf inhibits exchange of

336 water across the ice front. However over time, an increasing amount of cooler water is  
337 able to enter the ice shelf cavity, and is advected below the ice shelf (Figure 7).

338 The changing temperature flux into the ice shelf cavity in the center of the domain is  
339 partly driven by changing ocean velocities, observed at the ice front directly after the  
340 iceberg calves. The pre-calving meridional flow at the ice front is dominated by strong  
341 boundary currents moving water into and out of the ice shelf cavity along the flanks for  
342 the domain, while very little meridional velocity is observed in the center of the domain  
343 (as discussed in Section 4.1). After the iceberg calves, large meridional velocities are  
344 observed at the ice front (Figure 10). The structure and variability of the velocity field  
345 observed at the ice front after calving, suggest the elevated flow speed are driving by ocean  
346 instabilities that are triggered by the calving iceberg. These instabilities presumably a  
347 key driver of the enhanced vertical mixing described above. [How do these instabilities  
348 work?]

## 5.2. Inside the ice shelf cavity

349 The combination of cool sub-surface temperature anomalies and elevated ocean veloci-  
350 ties at the ice front, results in a temperature flux across the ice front, as cool temperatur-  
351 anomalies to enter the ice shelf cavity (Figure 7). Once the cooler water has entered the  
352 ice shelf cavity, the anomalies spread southwards within the ice shelf cavity, eventually  
353 reaching all the way to the grounding line. As the cool water spreads into the cavity, it  
354 mixes with the water within the ice shelf cavity, causing a reduction in the strength of  
355 the anomaly towards the grounding line (Figure 7c).

356 The cooling of the water inside the ice shelf cavity after calving leads to a reduction of  
357 the melt rates at the base of the ice shelf (Figure 9). The reduced melt rates occur over

358 a wide area extending from the newly calved ice front, all the way towards the grounding  
359 line. The negative melt rate anomalies increase over time, as more cold water enters the  
360 ice shelf cavity. The strongest negative anomalies are observed near the ice front, while  
361 the strength of the negative melt rate anomalies are reduced towards the grounding. The  
362 reduction in melt rates are up to 0.5 m per year, which is small compared to the mean  
363 melt rates near the grounding line, but is a substantial fraction of the melt at intermediate  
364 depths (Figure 5a).

365 Near the ice front, the competing effects of warm surface water subducting beneath the  
366 ice shelf on the flanks of the domain, and the cool water entering the ice shelf in the enter  
367 of the domain, lead to a complex of pattern of positive and negative melt rate anomalies  
368 within 20 km of the ice front (Figure 5). The strongest positive anomalies are observe on  
369 the western side of the ice shelf front, while the strongest negative melt rate anomalies  
370 are observed in the center of the domain. This is likely related to the geometry of the  
371 calving iceberg.

372 The changes in ice shelf melt rates following the calving event are primarily driven by  
373 changing ocean temperatures at the base of the ice shelf. In contrast the ocean velocities,  
374 and hence the frictional velocity at the ice base, remain largely unchanged after the calving  
375 event (see Figure S4 in the supplementary material), and do not play a large role in the  
376 changing melt rates.

377 The presence of a northern boundary in our simulation mean that we are unable to  
378 entirely remove the iceberg from the domain and observe the system approaching a new  
379 equilibrium state. However, a comparison between the iceberg calving simulation and  
380 the missing-iceberg simulation (where the model was spun up with the iceberg removed

from the start of the simulation) shows that after 60 days the hydrography inside the ice shelf cavity in the iceberg-calving simulation appears to be qualitatively similar to missing-iceberg simulation steady state (see Figure S3 in the supplementary material, for example). This suggests that the processes occurring at the ice front directly after calving are transient processes which allow the system to move towards a steady state that is largely controlled by the ice shelf geometry. Since the ice shelf geometry in our simulation is highly idealized, it is unclear whether the adjustment time scale seen here is relevant to real-world ice shelves.

### 5.3. Around the tabular iceberg

As the iceberg drifts through the water, it affects the ocean velocity and stratification in its immediate vicinity. As was seen near the ice front, the enhanced mixing around the iceberg causes warm salty anomalies around the iceberg near the surface, and cool fresh anomalies at depth (Figure 11a). As the iceberg drifts away from the ice shelf, the iceberg leaves a trail of warm surface anomalies in its wake that maps out the iceberg path of the iceberg (as discussed in Stern et al [2017]) (Figure 2c). Similarly, cool subsurface temperature anomalies are observed in the wake of the iceberg at depth (not shown).

Strong barotropic ocean currents are observed directly below the iceberg as it drifts through the water (Figure 11b). The column of uniform velocity below the iceberg is evidence of the Taylor column that forms below the iceberg. The sudden changing in ocean thickness when moving from below the iceberg to the open ocean causes a dynamical barrier which separates the flow beneath the iceberg from the rest of water column (as was seen across the ice front). Similar Taylor columns have been observed above sea mounts [reference]. Elevated largely barotropic flows are observed around the iceberg as it drifts.

403 These currents are a result of complex interaction between the iceberg on the surrounding  
404 ocean. More work is needed (perhaps in a further idealized setting) to understand these  
405 interactions.

406 Directly below the iceberg on the ocean floor, an increased diapycnal mixing is observed  
407 in the bottom boundary layer. This elevated mixing in the bottom boundary layer is  
408 likely a result of a barotropic adjustment driven by the iceberg motion. As the iceberg  
409 drifts through the water, the region of elevated diapycnal mixing shifts so that it remains  
410 directly below the iceberg. Similarly elevated rates in diapycnal mixing are observed at the  
411 bottom of the water column near the ice front.

## 6. Conclusion

412 This study presents a new Lagrangian framework for modeling sub-ice-shelf cavities. In  
413 this framework, the ice shelf is constructed out of many Lagrangian elements, which are  
414 bonded together by numerical bonds. By breaking the bonds, we can use the Lagrangian  
415 model to simulate iceberg calving, and to observe the ocean response to large calving  
416 events (Figures 2). This capability is currently not possible using more traditional Eulerian  
417 models [Stern et al., 2017].

418 We validate the Lagrangian ice shelf model by simulating the flow beneath a (static)  
419 idealized ice shelf, and comparing the results to an existing Eulerian model simulations  
420 with identical configuration. The results from the static ice shelf simulation using the  
421 Lagrangian ice-shelf model fit within our paradigm of understanding for circulation within  
422 ice-shelf cavities: buoyant meltwater that enters the ice-shelf cavity drives freshwater  
423 plumes at the ice-shelf base, which drives the circulation within the cavity. The circulation,  
424 melt rates and ocean hydrography achieved using the Lagrangian ice shelf compare well

425 with other simulations in the MISOMIP experiments. Comparing the results to the results  
426 obtained using an Eulerian model in an identical static configuration showed that the  
427 two models simulations are very similar. Small differences between the Lagrangian and  
428 Eulerian ice shelves models result from interpolation errors, but these errors are two  
429 orders of magnitude smaller than typical difference observe between simulations using  
430 different ocean models (for example). Demonstrating that the Lagrangian ice-shelf model  
431 is able to reproduce the results of an Eulerian ice-shelf model in the same static ice-shelf  
432 configuration is a prerequisite developing more advanced Lagrangian ice-shelf models and  
433 represents a good benchmark test for new Lagrangian ice-shelf models.

434 The Lagrangian model is then used to simulate iceberg calving. In the iceberg calving  
435 experiment, enhanced ocean mixing is observed near the ice front and around the tabular  
436 iceberg after the iceberg detaches from the ice shelf. The enhanced mixed brings warm  
437 water to the surface, leading to a warming of sea surface temperatures around the iceberg  
438 and ice front. The mixing allow leads to a cooling of sub-surface waters near the ice front.  
439 These cooler waters enter the ice shelf cavity and lead to reduced melt rates at the base  
440 of the ice shelf in the months following the calving event.

## 7. To dos

### 7.1. Things to add:

- 441 1) Time series showing variably quantities at points in the domain (e.g.: temperature  
442 flux, velocity, total melt...)
- 443 2) Some aggregated numbers to emphasis some ideas (e.g.: Total change in melt volume  
444 and circulation....)

445 3) Add some perspectives to the Conclusion/Discussion about whether we can trust the  
446 results shown here.

447

## 7.2. New/Improv'd figures

448 1) Figure 11, domesticating below the iceberg (Temperature, velocity, kd (many v too)).  
449 2) Time series figure 3) Ocean velocity snapshots xz 4) Ocean velocity snapshots yz  
450 (maybe) 3) Late time figure (maybe - see supp)

## 7.3. Some other points to perhaps include

451 1) The no-bonds simulation and the fixed velocity simulation both show the same sur-  
452 face warming and subsurface cooling signals, indicating that this is quite a robust feature.

453

454 2) The fact that the warming/cooling is seen directly around the calving iceberg (see  
455 following video) indicates that the mechanism is a local mechanism rather than a global  
456 basin adjustment

457

458 3) The changes in melt appear to tend towards the results from the Broken Shelf simu-  
459 lation, suggesting local processes around the iceberg causing warming/cooling, help the  
460 system to move between steady states, which are imposed by the large scale geometry  
461 and forcing.

462

463 4) Looking at Kd shows largest mixing regions occur in places where there is open water.  
464 No enhanced Kd is observed below the iceberg (because it is too deep). This suggests

465 that changes in mixing are caused by new regions being exposed to open water (i.e.: wind).

466

467 5) A simulation using no sub-ice shelf friction has a very similar signal, suggesting that

468 the signal is not caused my iceberg induced mixing.

469

470 6) Is the enhanced mixing at the bottom of the water column around the iceberg re-

471 lated to the warming/cooling signal? Why is it there at all?

472

473

#### 7.4. Other questions:

474 1) What is happening with the enhanced mixing exactly? It looks like it is driven by  
475 new area being exposed to open water. But does this make sense? When an iceberg  
476 moves, where does the water which takes its place come from?

477 2) Does the surface warming and subsurface cooling have to be a result of enhanced  
478 mixing? Is it possible that mixing is occurring even though  $k_d$  is small? Possibilities:

479

## References

- 480 Asay-Davis, X. S., S. L. Cornford, B. K. Galton-Fenzi, R. M. Gladstone, G. H. Gudmundsson, D. M. Holland, P. R. Holland, and D. F. Martin (2016), Experimental design for  
481 three interrelated marine ice sheet and ocean model intercomparison projects: MIS-  
482 MIP v. 3 (MISMIP+), ISOMIP v. 2 (ISOMIP+) and MISOMIP v. 1 (MISOMIP1).  
483 *Geoscientific Model Development* 9, no. 7: 2471.
- 484 Arrigo, K. R., G. L. van Dijken, D. G. Ainley, M. A. Fahnestock, and T. Markus (2002).  
485 Ecological impact of a large Antarctic iceberg. *Geophys. Res. Lett.*, 29(7).
- 486 Alley, R. B., H. J. Horgan, I. Joughin, K. M. Cuffey, T. K. Dupont, B. R. Parizek, S.  
487 Anandakrishnan, and J. Bassis (2008), A simple law for ice-shelf calving. *Science* 322,  
488 no. 5906, 1344-1344.
- 489 Bassis, J. N., and S. Jacobs (2013), Diverse calving patterns linked to glacier geometry.  
490 *Nature Geoscience*, 6(10), 833-836.
- 491 Benn, D. I., C. R. Warren, and R. H. Mottram (2007). Calving processes and the dynamics  
492 of calving glaciers. *Earth-Science Reviews*, 82(3), 143-179.
- 493 Bigg, G. R., Wadley, M. R., Stevens, D. P., and Johnson, J. A. (1997), Modeling the  
494 dynamics and thermodynamics of icebergs. *Cold Regions Science and Technology*, 26(2),  
495 113-135.
- 496 Borstad, C. P., A. Khazendar, E. Larour, M. Morlighem, E. Rignot, M. P. Schodlok, and  
497 H. Seroussi (2012), A damage mechanics assessment of the Larsen B ice shelf prior to  
498 collapse: Toward a physically-based calving law, *Geophys. Res. Lett.*, 39, L18502
- 499 Biddle, L. C., J. Kaiser, K. J. Heywood, A. F. Thompson and A. Jenkins (2015), Ocean  
500 glider observations of iceberg-enhanced biological productivity in the northwestern Wed-

- 502 dell Sea, *Geophys. Res. Lett.*, 42, 459465.
- 503 De Rydt, J., and G. H. Gudmundsson (2016), Coupled ice shelf ocean modeling and  
504 complex grounding line retreat from a seabed ridge. *J. of Geophys. Res.: Earth Surface*,  
505 121(5), 865-880.
- 506 Dunne, J.P., J.G. John,, A.J. Adcroft, S.M. Griffies, R.W. Hallberg, E. Shevliakova,  
507 R.J. Stouffer, W. Cooke, K.A. Dunne, M.J Harrison, and J.P. Krasting (2012), GFDL's  
508 ESM2 global coupled climate-carbon Earth System Models. Part I: Physical formulation  
509 and baseline simulation characteristics. *J. of Climate*, 25(19), 6646-6665.
- 510 Depoorter, M. A., J. L. Bamber, J. A. Griggs, J. T. M. Lenaerts, Stefan RM Ligtenberg,  
511 M. R. van den Broek, and G. Moholdt (2013), Calving fluxes and basal melt rates of  
512 Antarctic ice shelves. *Nature*, 502(7469), 89-92.
- 513 Determan J., Gerdes R. (1994), Melting and freezing beneath ice shelves: implications  
514 from a three-dimensional ocean-circulation model. *Ann. Glaciol.*, 20, 413-419.
- 515 Dowdeswell, J. A., and J. L. Bamber (2007), Keel depths of modern Antarctic icebergs  
516 and implications for sea-floor scouring in the geological record. *Marine Geology*, 243(1),  
517 120-131.
- 518 Duprat, L. P., G. R. Bigg, and D. J. Wilton (2016), Enhanced Southern Ocean marine  
519 productivity due to fertilization by giant icebergs. *Nature Geoscience*.
- 520 Eckert, E. R. G. (1950). Introduction to the Transfer of Heat and Mass. McGraw-Hill.
- 521 Gladstone, R. M., G. R. Bigg, and K. W. Nicholls. (2001), Iceberg trajectory modeling  
522 and meltwater injection in the Southern Ocean (19782012). *J. of Geophys. Res.: Oceans*,  
523 106(C9), 19903-19915.

- 524 Goldberg, D. N., C. M. Little, O. V. Sergienko, A. Gnanadesikan, R. Hallberg, and M.  
525 Oppenheimer (2012), Investigation of land ice?ocean interaction with a fully coupled  
526 ice-ocean model: 1. Model description and behavior. *J. of Geophys. Res.: Earth Surface*,  
527 117(F2).
- 528 Gladish, C. V., D. M. Holland, P. R. Holland, and S. F. Price (2012), Ice-shelf basal  
529 channels in a coupled ice/ocean model. *J. of Glaciol.*, 58(212), 1227-1244.
- 530 Grosfeld K., R. Gerdes, J. Determan (1997), Thermohaline circulation and interaction  
531 between ice shelf cavities and the adjacent open ocean. *J. Phys. Oceanogr.*, **102**, C7,  
532 15959-15610.
- 533 Grosfeld, K., and H. Sandhger, (2004). The evolution of a coupled ice shelfocean system  
534 under different climate states. *Global and Planetary Change*, 42(1), 107-132.
- 535 Hallberg, R., A. Adcroft, J. P. Dunne, J. P., Krasting, R. J., and Stouffer (2013), Sensitiv-  
536 ity of twenty-first-century global-mean steric sea level rise to ocean model formulation.  
537 *J. of Climate*, 26(9), 2947-2956.
- 538 Holland D. M., Jenkins A. (2001), Adaptation of an isopycnic coordinate ocean model for  
539 the study of circulation beneath ice shelves. *Mon. Wea. Rev.*, 129, 1905-1927.
- 540 Holland P. R. and D. L. Feltham (2006), The effects of rotation and ice shelf topography  
541 on frazil-laden Ice Shelf Water plumes. *J. Phys. Oceanogr.*, 36, 2312-2327.
- 542 Holland, D. M., and A. Jenkins (1999), Modeling thermodynamic ice-ocean interactions  
543 at the base of an ice shelf. *J. of Phys. Oceanogr.* 29.8, 1787-1800.
- 544 Hellmer H.H., Olbers D. J. (1989), A two-dimensional model for the thermohaline circu-  
545 lation under an ice shelf. *Antarctic Science*, 1, 325- 336.

- 546 Hopkins, M. A. (1996). On the mesoscale interaction of lead ice and floes. *J. of Geophys.*  
547 *Res.: Oceans*, 101(C8), 18315-18326.
- 548 Jakobsen, T. (2001). Advanced character physics. In *Game Developers Conference*, Vol.  
549 3.
- 550 Jenkins, A., P. Dutrieux, S. S. Jacobs, S. D. McPhail, J. R. Perrett, A. T. Webb, and  
551 D. White (2010), Observations beneath Pine Island Glacier in West Antarctica and  
552 implications for its retreat. *it Nature Geo.*, 3(7), 468-472.
- 553 Jacobs, S. S., A. Jenkins, C. F. Giulivi, and P. Dutrieux (2011). Stronger ocean circulation  
554 and increased melting under Pine Island Glacier ice shelf. *Nature Geo.*, 4(8), 519-523.
- 555 Jongma, J. I., E. Driesschaert, T. Fichefet, H. Goosse, and H. Renssen (2009), The effect of  
556 dynamic-thermodynamic icebergs on the Southern Ocean climate in a three-dimensional  
557 model, *Ocean Modell.*, 26, 104113.
- 558 Lewis E.L. and R.G. Perkin (1986), Ice pumps and their rates. *J. of Geophys. Res.*, 91,  
559 11756-11762.
- 560 Losch, M. (2008). Modeling ice shelf cavities in az coordinate ocean general circulation  
561 model. *J. of Geophys. Res.: Oceans*, 113(C8).
- 562 Li, B., H. Li, Y. Liu, A. Wang and S. Ji (2014), A modified discrete element model for  
563 sea ice dynamics. *Acta Oceanologica Sinica*, 33(1), 56-63.
- 564 Liu, M. B. and G. R. Liu (2010), Smoothed particle hydrodynamics (SPH): an overview  
565 and recent developments. *Archives of computational methods in engineering*, 17(1), 25-  
566 76.
- 567 Lichy, C., and H. H. Hellmer (2001). Modeling giant-iceberg drift under the influence of  
568 sea ice in the Weddell Sea, Antarctica. *J. of Glaciol.*, 47(158), 452-460.

- 569 Levermann, A., T. Albrecht, R. Winkelmann, M. A. Martin, M. Haseloff, and I. Joughin.  
570 (2012), Kinematic first-order calving law implies potential for abrupt ice-shelf retreat.  
571 *The Cryosphere*, 6(2), 273-286.
- 572 Martin, T., and Adcroft, A. (2010), Parameterizing the fresh-water flux from land ice  
573 to ocean with interactive icebergs in a coupled climate model. *Ocean Modelling*, 34(3),  
574 111-124.
- 575 Marsh, R., V. O. Ivchenko, N. Skliris, S. Alderson, G. R. Bigg, G. Madec, A. T. Blaker  
576 Y. Aksenov, B. Sinha, A.C. Coward, and J.L. Sommer (2015), NEMOICB (v1. 0):  
577 interactive icebergs in the NEMO ocean model globally configured at eddy-permitting  
578 resolution. *Geoscientific Model Development* 8, no. 5 (2015): 1547-1562.
- 579 MacAyeal D.R. (1984), Thermohaline Circulation Below the Ross Ice Shelf: A Conse-  
580 quence of Tidally Induced Vertical Mixing and Basal Melting. *J. Geophys. Res.*, 89,  
581 597-606
- 582 Nicholls K.W. (1996), Temperature variability beneath Ronne Ice Shelf, Antarctica, from  
583 thermistor cables. *J. Phys. Oceanogr.*, 11, 1199-1210.
- 584 Nicholls KW, Østerhus S, Makinson K (2009), Ice-Ocean processes over the continental  
585 shelf of the southern Weddell Sea, Antarctica: a review. *Rev. Geophys.* 47(3).
- 586 Omelyan, I. P., M. I. Mryglod, and R. Folk (2002), Optimized Verlet-like algorithms for  
587 molecular dynamics simulations. *Physical Review E*, 65(5), 056706.
- 588 Rignot, E., S. Jacobs, J. Mouginot, and B. Scheuchl (2013), Ice-shelf melting around  
589 Antarctica. *Science*, 341, no. 6143 (2013): 266-270.
- 590 Robinson, N. J., and Williams, M. J. M. (2012). Iceberg-induced changes to polynya  
591 operation and regional oceanography in the southern Ross Sea, Antarctica, from in situ

- 592 observations. *Antarctic Science*, 24(5), 514-526.
- 593 Pan, W., A. M. Tartakovsky, and J. J. Monaghan (2013). Smoothed particle hydrody-  
594 namics non-Newtonian model for ice-sheet and ice-shelf dynamics. *J. of Comp. Phys.*,  
595 242, 828-842.
- 596 Pralong, A., and M. Funk (2005), Dynamic damage model of crevasse opening and appli-  
597 cation to glacier calving, *J. Geophys. Res.*, 110, B01309.
- 598 Seroussi H., Y. Nakayama, E.Y. Larour, D. Menemenlis, M. Morlighem, E. Rignot, and A.  
599 Khazendar (2017), Continued retreat of Thwaites Glacier, West Antarctica, controlled  
600 by bed topography and ocean circulation, *Geophys. Res. Lett.*, 44
- 601 Sergienko, O. V. (2013). Basal channels on ice shelves. *J. of Geophys. Res.: Earth Surface*,  
602 118(3), 1342-1355.
- 603 Silva, T. A. M., Bigg, G. R., and Nicholls, K. W. (2006), Contribution of giant icebergs  
604 to the Southern Ocean freshwater flux. *J. of Geophys. Res.: Oceans*, 111(C3).
- 605 Smith, K., B. Robison, J. Helly, R. Kaufmann, H. Ruhl, H., T. Shaw, and M. Vernet  
606 (2007), Free-drifting icebergs: Hotspots of chemical and biological enrichment in the  
607 Weddell Sea, *Science*, 317, 478482.
- 608 Stern, A. A., D. M. Holland, P. R. Holland, A. Jenkins and J. Sommeria (2014), The effect  
609 of geometry on ice shelf ocean cavity ventilation: a laboratory experiment. *Experiments*  
610 *in Fluids*, 55(5), 1-19.
- 611 Stern, A.A., Johnson, E., Holland, D.M., Wagner, T.J., Wadhams, P., Bates, R., Abra-  
612 hamsen, E.P., Nicholls, K.W., Crawford, A., Gagnon, J. and Tremblay, J.E. (2015),  
613 Wind-driven upwelling around grounded tabular icebergs. *J. of Geophys. Res.: Oceans*,  
614 120(8), 5820-5835.

- 615 Stern, A. A., A. Adcroft, and O. Sergienko (2016), The effects of Antarctic iceberg calv-  
616 ing?size distribution in a global climate model. *J. of Geophys. Res.: Oceans*, 121(8),  
617 5773-5788.
- 618 Stern, A. A., A. Adcroft, O. Sergienko, G. Marques, R. Hallberg (2017), Modeling tabular  
619 icebergs coupled to an ocean model. *Ocean Modeling*
- 620 Swope, W. C., H. C. Andersen, P. H. Berens, and K. R. Wilson (1982), A computer  
621 simulation method for the calculation of equilibrium constants for the formation of  
622 physical clusters of molecules: Application to small water clusters. *The Journal of  
623 Chemical Physics* 76, no. 1, 637-649.
- 624 Tournadre, J., N. Bouhier, F. Girard-Ardhuin, and F. Rmy (2016), Antarctic icebergs  
625 distributions 1992-2014. *J. Geophys Res: Oceans*.
- 626 Vernet, M., et al. (2012), Islands of ice: Influence of free-drifting Antarctic icebergs on  
627 pelagic marine ecosystems, *Oceanography*, 25(3), 3839
- 628 Weeks, W. F., and W. J. Campbell (1973). Icebergs as a fresh-water source: an appraisal.  
629 *J. of Glaciol.*, 12(65), 207-233.
- 630 White, L., A. Adcroft, and R. Hallberg (2009), High-order regriddingremapping schemes  
631 for continuous isopycnal and generalized coordinates in ocean models. *J. of Comp.  
632 Phys.*, 228(23), 8665-8692.

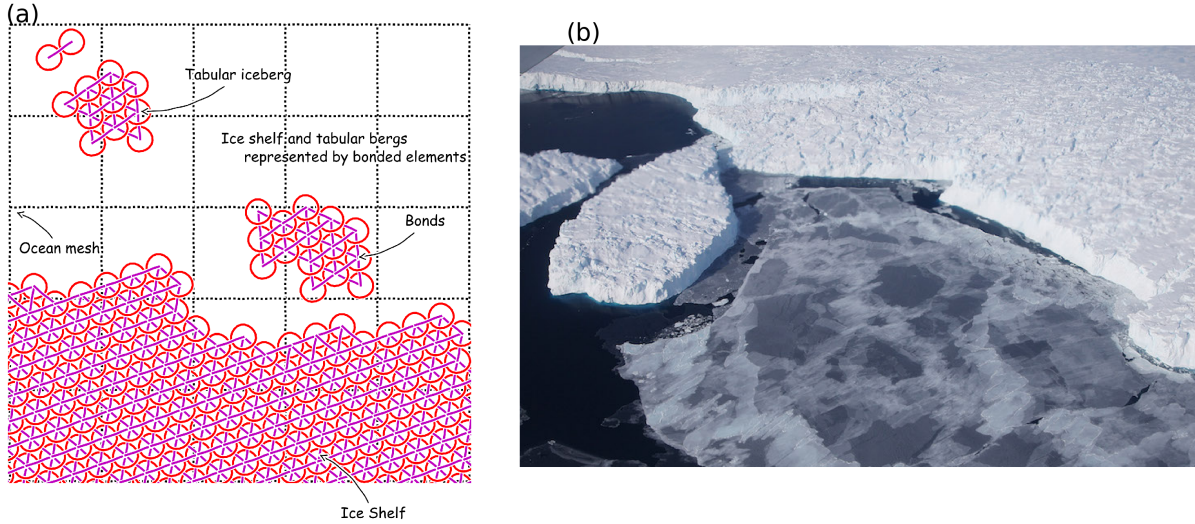


**Figure 1.** Schematic showing how ice shelves and tabular icebergs are constructed using Lagrangian elements. (a) Schematic of multiple ice elements that are joined together by numerical bonds (magenta lines) to form larger structures such as ice shelves and tabular icebergs. These numerical elements have finite extent and are able to interact with the ocean across multiple grid cells, and can interact with other elements. (b) Areal photograph of an ice shelf and tabular iceberg with elements superimposed over it to illustrate how the Lagrangian elements can be used to model ice shelves and tabular icebergs. In this schematic the ice elements (purple dots) are initialized in a staggered lattice covering the surface area of the iceberg. For purposes of mass aggregation, the ice elements are assumed to have hexagonal shape (red hexagons). For purposes of element interactions, the ice elements are assumed to be circular (black circles). Elements are initially bonded to adjacent elements using numerical bonds (magenta lines). These numerical bonds form equilateral triangles which give the shape rigidity. An ocean grid has been included (dashed cyan lines).

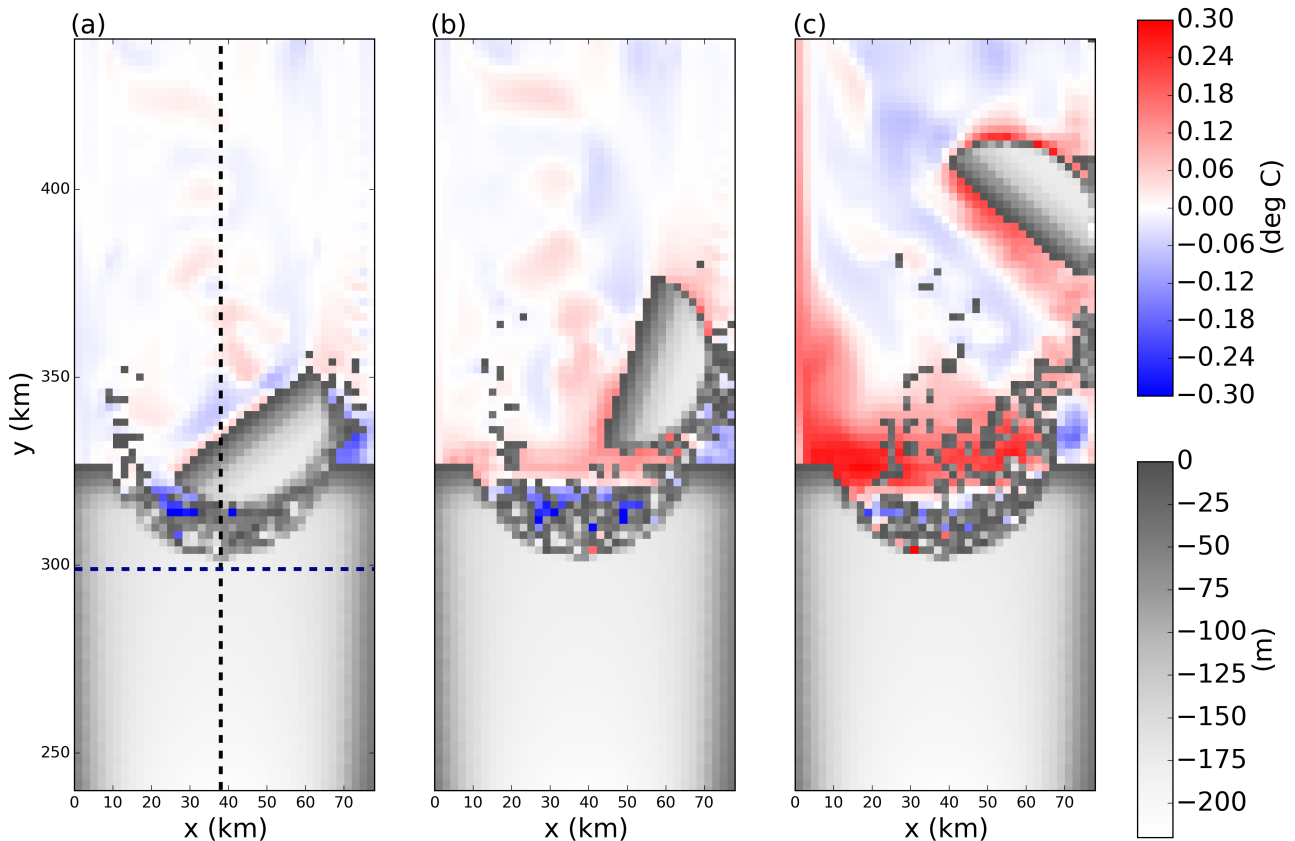


**Figure 2.** Snapshots of sea surface temperature anomalies in the iceberg calving simulation.

The anomalies are relative to pre-calving temperatures. Snapshots are taken (a) 7, (b) 15, and (c) 50 days after calving. Grid cells with ice mass  $> 10^4$  kg are plotted in white, with grey shading indicating thinner ice. The black and blue dashed line in panel (a) shows the location of the vertical transects shown in Figures 7 and 8, respectively

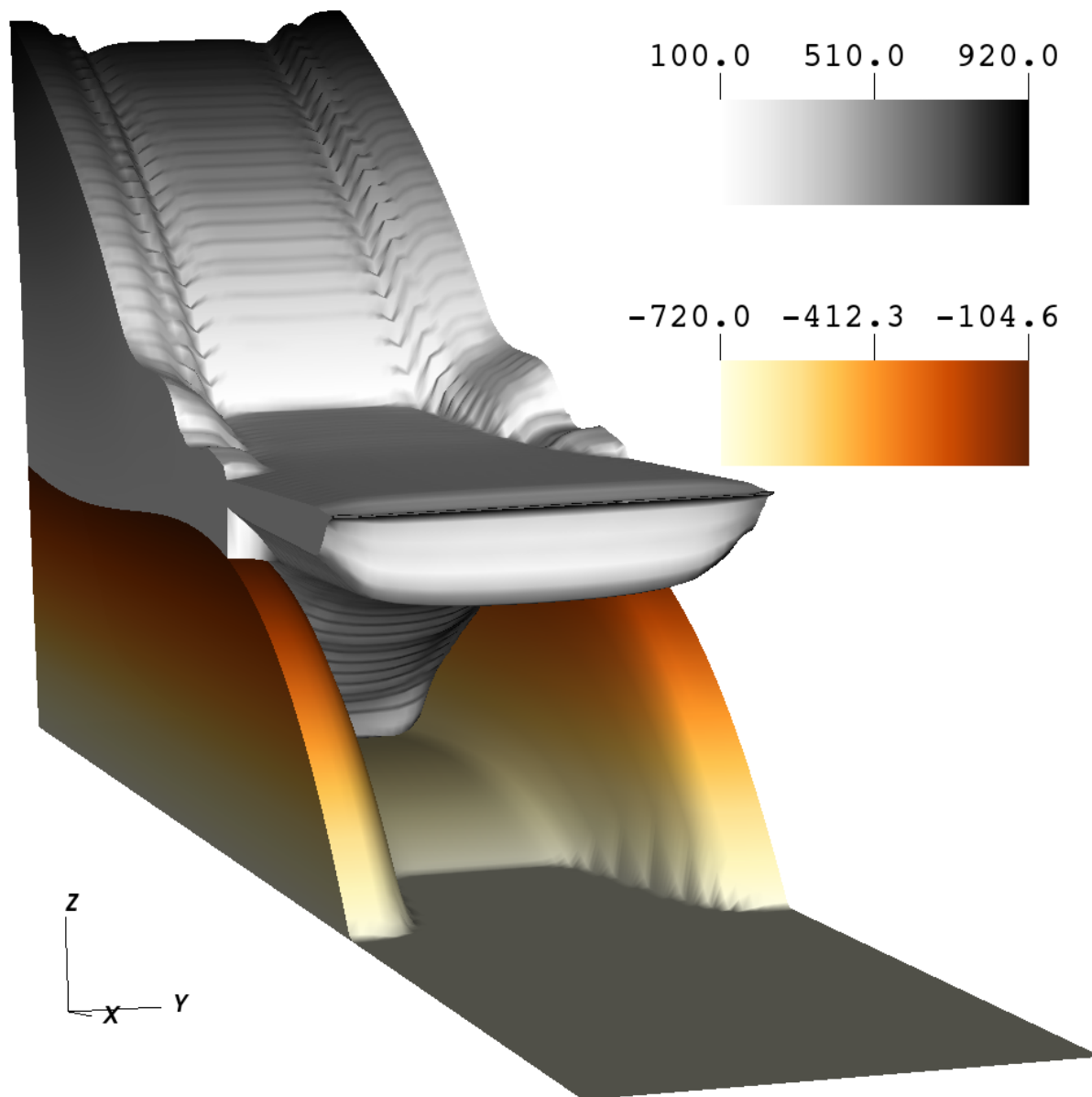


**Figure 3.** Ocean bottom topography and ice-shelf draft used in the Lagrangian and Eulerian static ice-shelf simulations

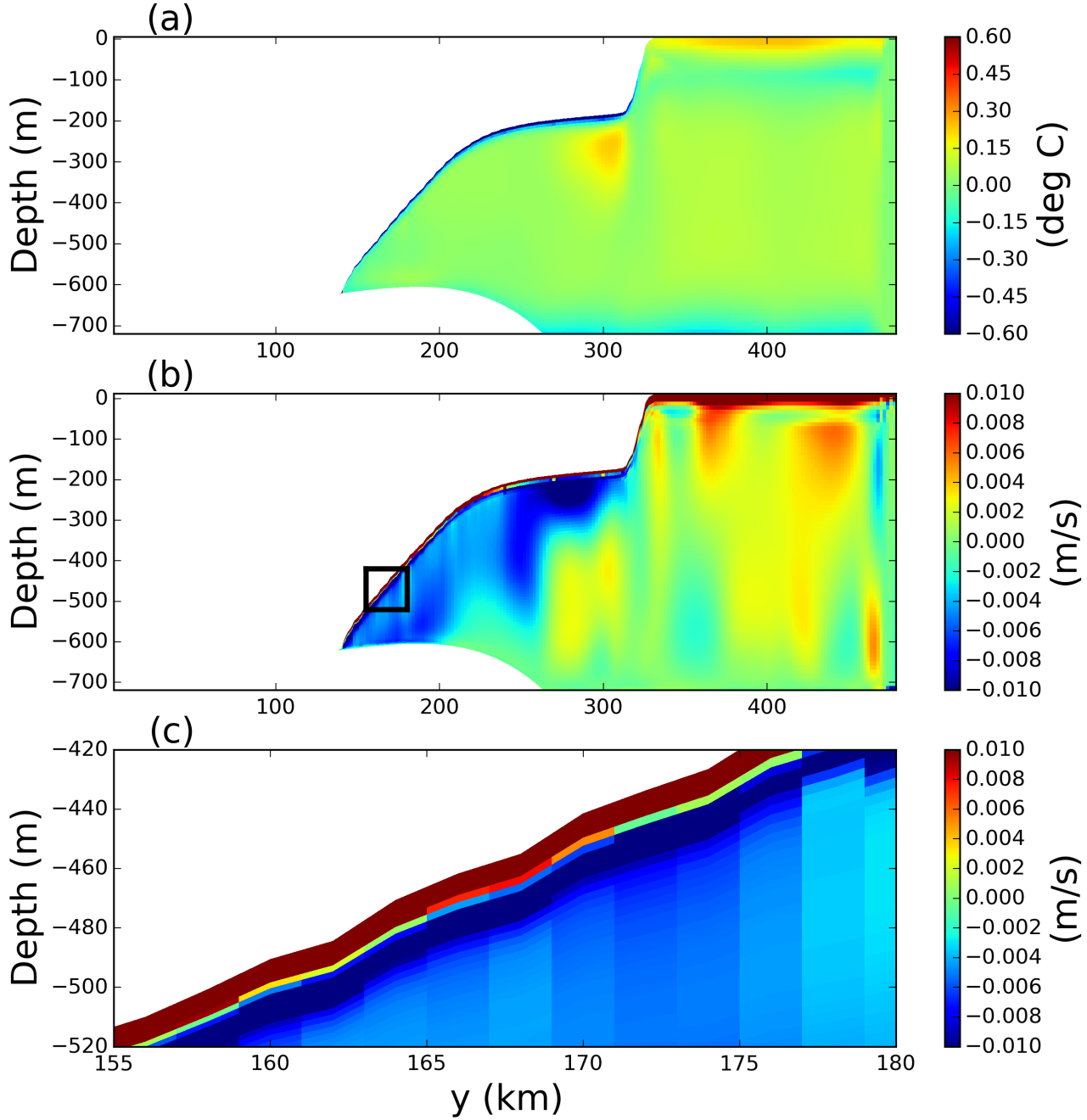


**Figure 4.** Snapshots of the static ice-shelf experiment taken after 5 years of model simulation, using the Lagrangian ice-shelf model coupled to the MOM6 ocean model. Panels show cross sections of the (a) ocean temperature anomaly relative the the initial temperature, and (b) the meridional ocean velocity. Panel (c) again shows the meridional ocean velocity, and is zoomed into the region near the ice-shelf base (the zoomed-in region is indicated with a black box (b)).

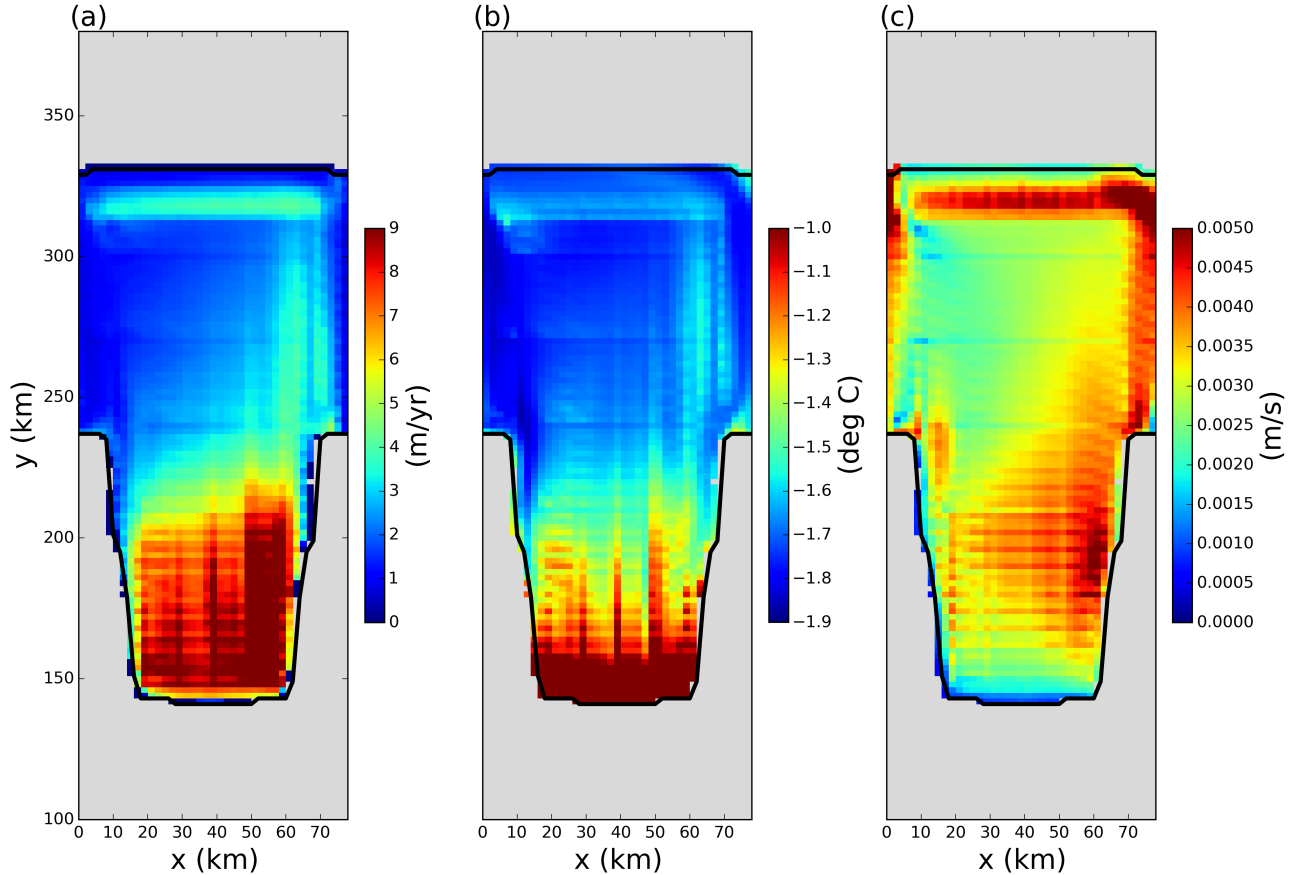


**Figure 5.** Results of the static ice-shelf experiment using the Lagrangian ice-shelf model coupled to MOM6. The three panels show 5 year time average of the (a) melt rate, (b) top-of-ocean temperature and (c) frictional velocity,  $u^*$ , at the base of the ice shelf. Fields are only shown in regions where the ice area fraction is  $\geq 0.8$ .

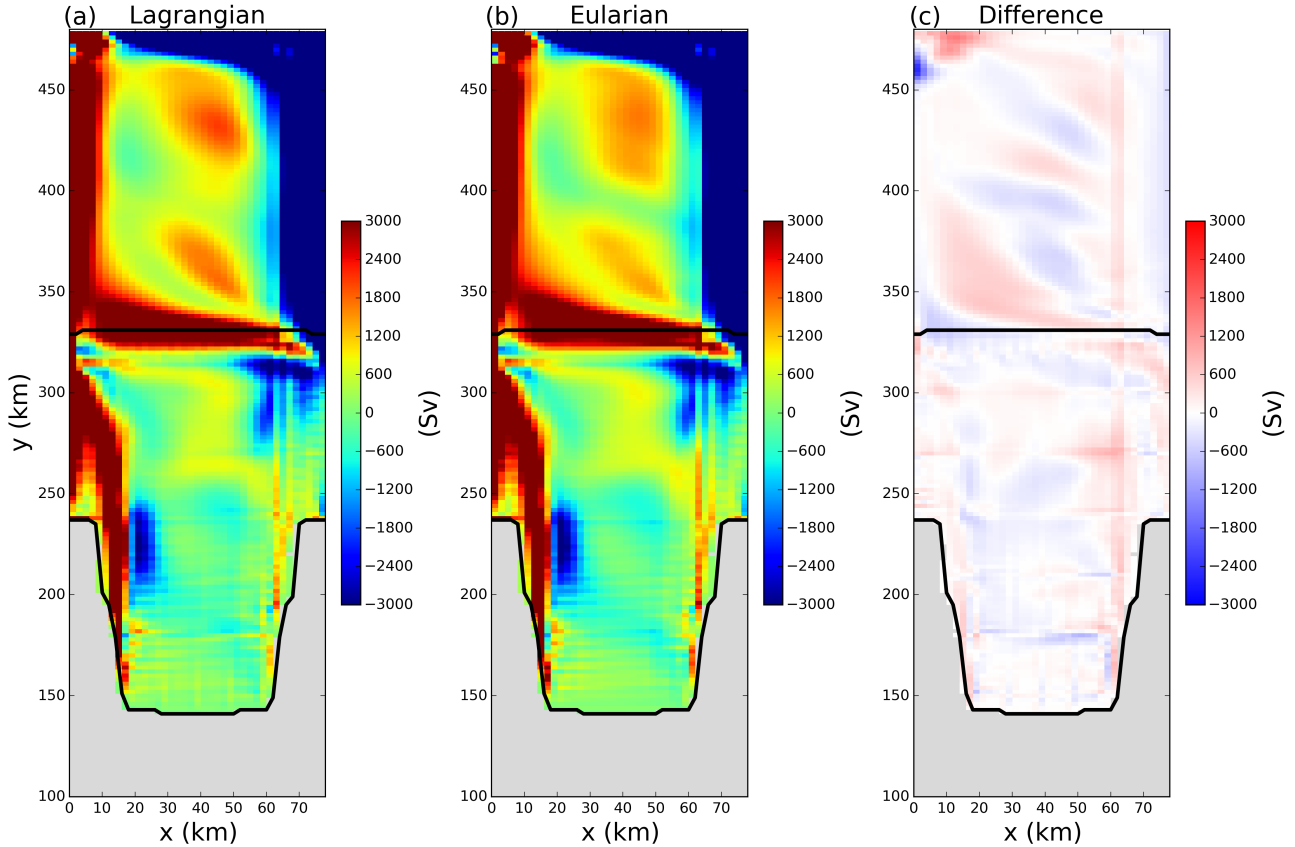


**Figure 6.** Time-averaged barotropic stream function in the (a) Lagrangian and (b) Eulerian simulations in the static ice-shelf configuration. Panel (c) shows the difference between panels (a) and (b). The time averages are taken over 5 years of model time, beginning at the end of the 5 year spin up period.

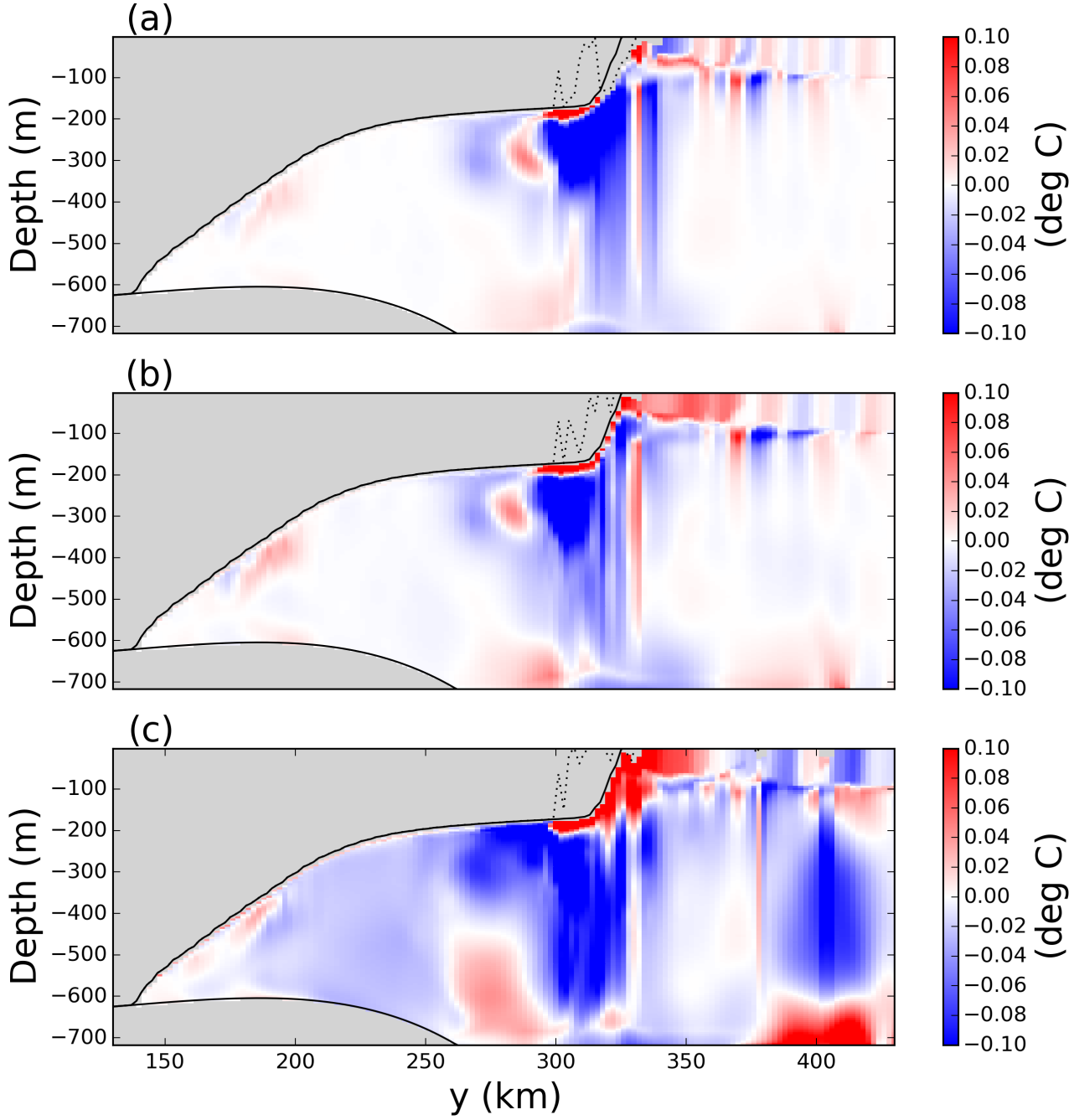


**Figure 7.** Snapshots of vertical sections of ocean temperature anomaly at  $x=40$  km in the iceberg-calving experiment. The anomalies are relative to pre-calving temperatures. Snapshots are taken (a) 7, (b) 15, and (c) 50 days after calving. In each panel, the base of the ice before calving and at the time of the snapshot are shown by the solid and dashed black lines, respectively. Positions that were not the ocean interior at in both snapshots are masked in grey. The position of the vertical transects is shown by the black dashed lines in Figure 2a.

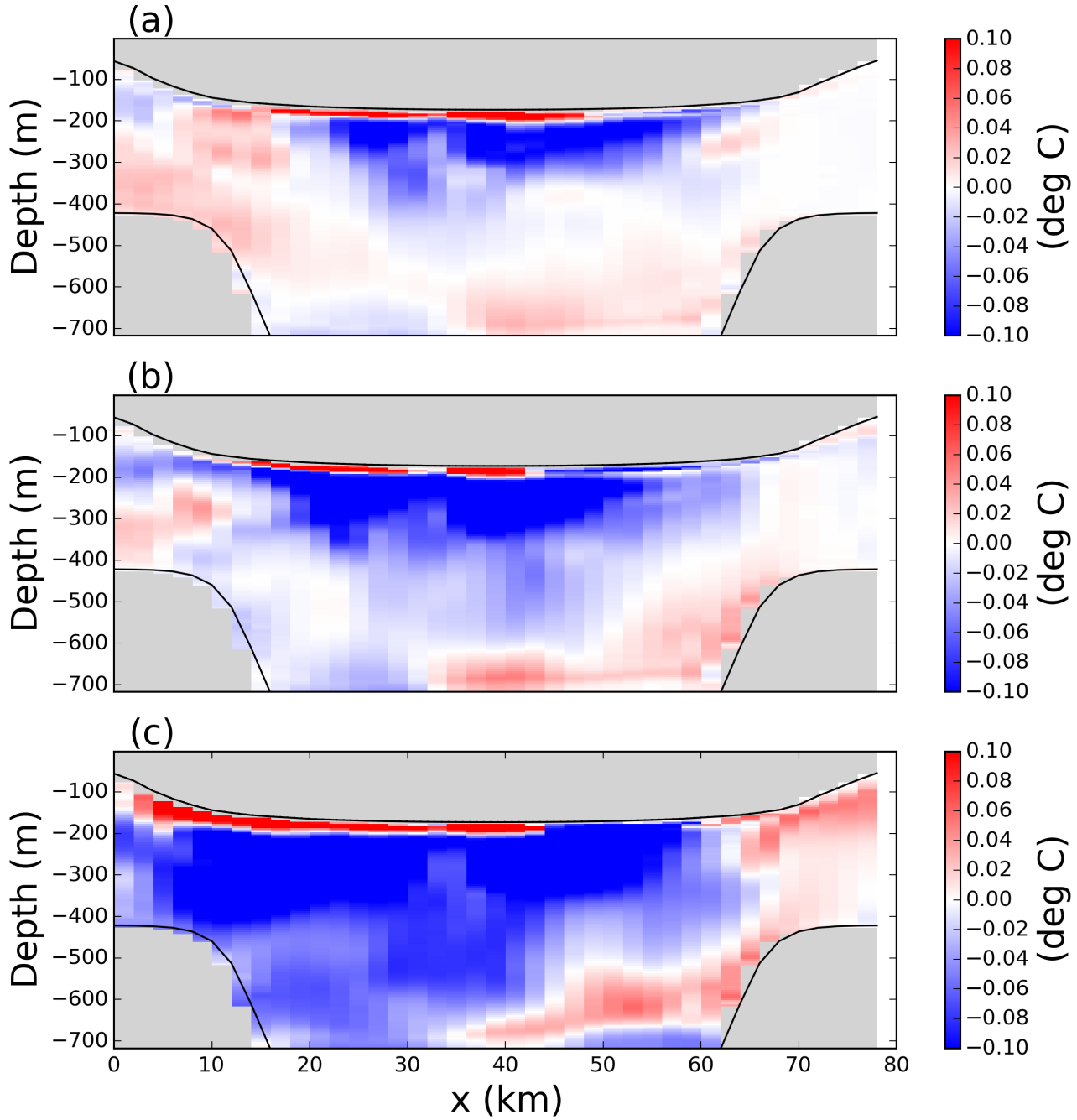


**Figure 8.** Snapshots of vertical sections of ocean temperature anomaly at  $y=300$  km in the tabular-iceberg-calving experiment. The anomalies are relative to pre-calving temperatures. Snapshots are taken (a) 7, (b) 15, and (c) 50 days after calving. The position of the vertical transects is shown by the blue dashed lines in Figure 2a.

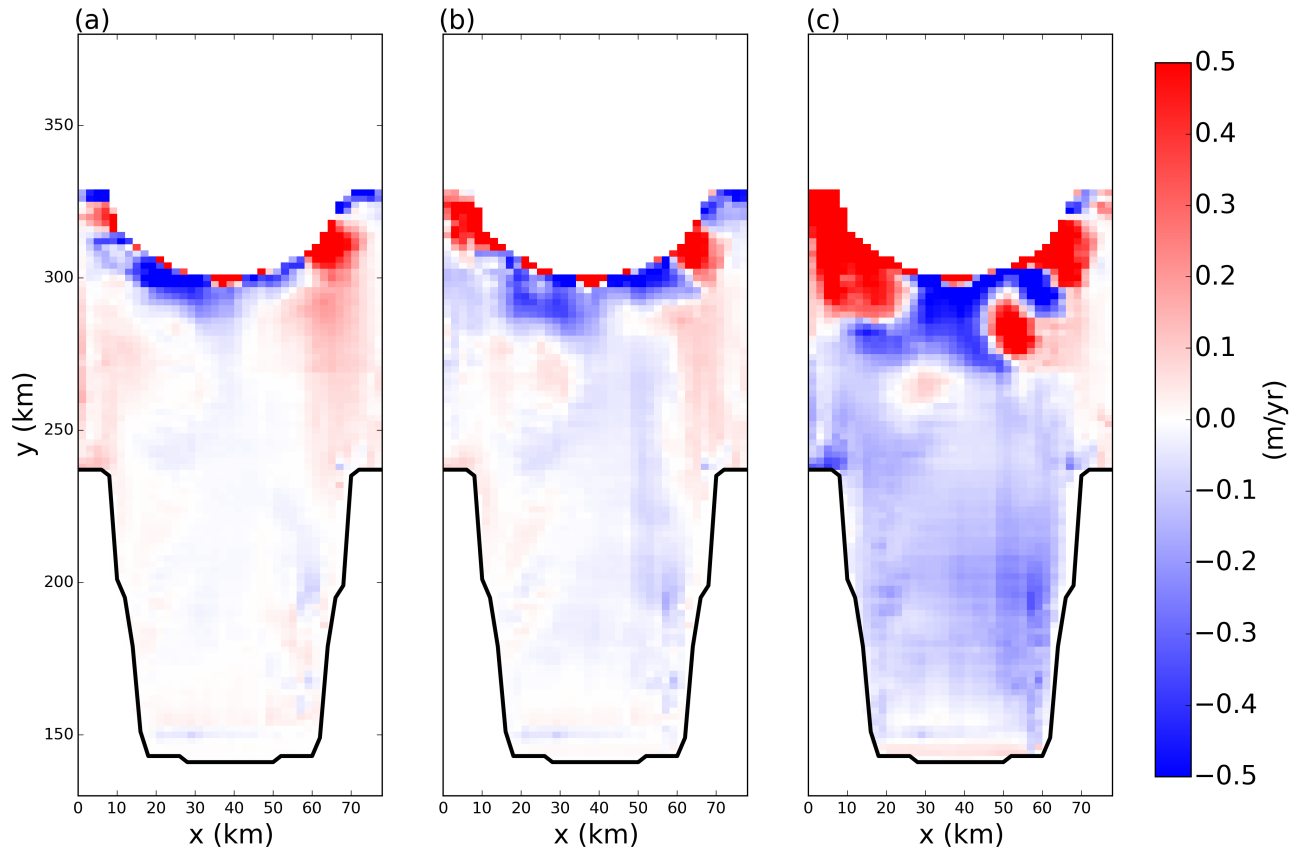


**Figure 9.** Snapshots of the melt rate anomaly, at the ice-shelf base in the tabular iceberg calving simulation. The anomalies are relative to pre-calving temperatures. Snapshots are taken (a) 7, (b) 15, and (c) 50 days after calving.

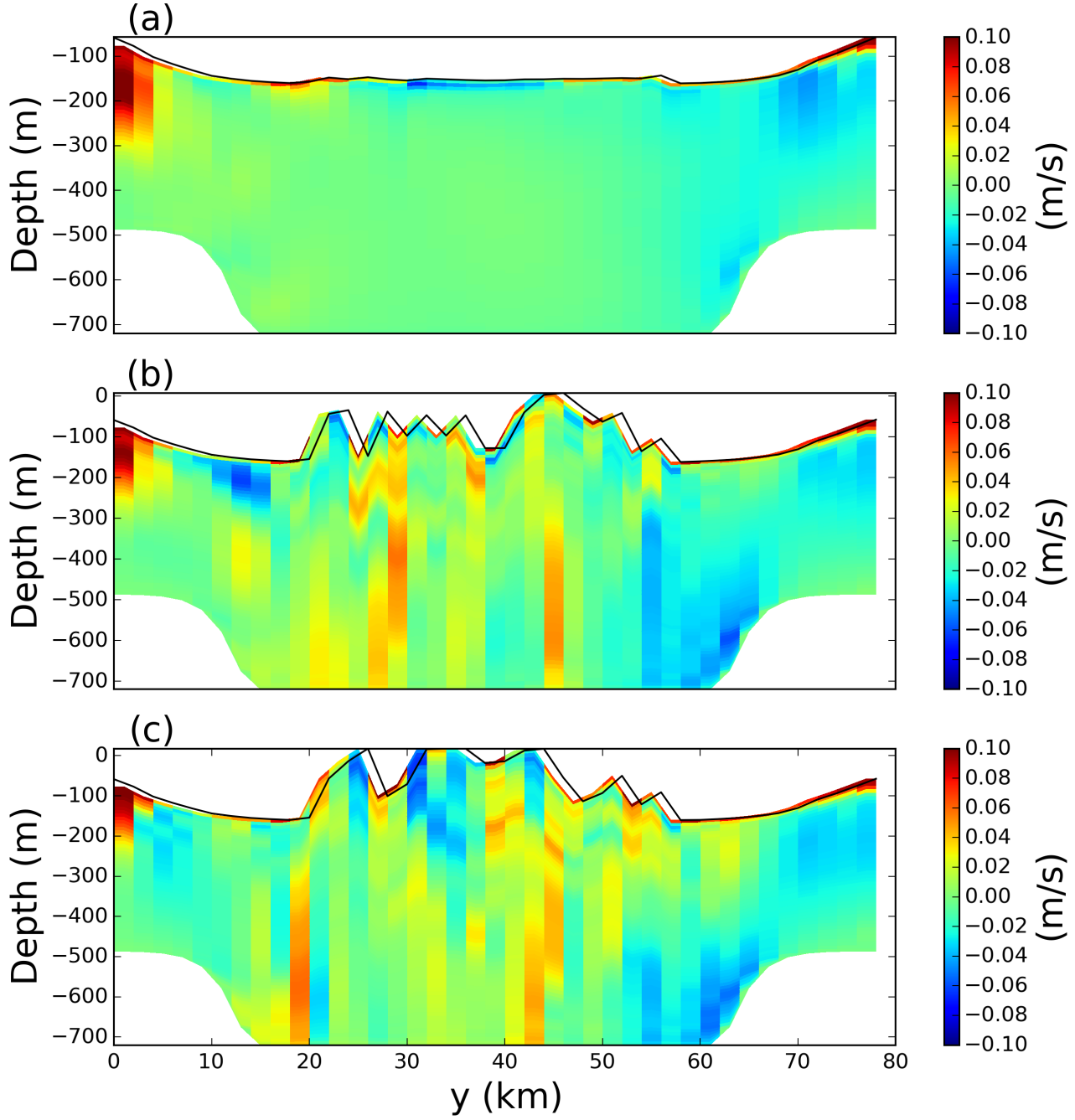


**Figure 10.** Snapshots of vertical sections of meridional velocity anomaly at  $y=300$  km in the tabular-iceberg-calving experiment. The anomalies are relative to pre-calving temperatures. Snapshots are taken (a) 7, (b) 15, and (c) 50 days after calving. The position of the vertical transects is shown by the blue dashed lines in Figure 2a.

**Figure 11.** Snapshots of vertical sections of ocean (i) temperature anomaly, (ii) meridional velocity, and (iii) dipycnal diffusivity at  $y=???$  km in the tabular-iceberg-calving experiment. The anomalies are relative to pre-calving temperatures. Snapshots are taken (a) 7, (b) 15, and (c) 50 days after calving. The position of the vertical transects is shown by the ??? dashed lines in Figure 2a.

**Figure 12.** Time series of temperature fluxes, velocities, melt rates....

Parameter	Symbol	Value	Unit
Domain Length	$L_x$	80	km
Domain Width	$L_y$	480	km
Horizontal Resolution	$\Delta x$	2	km
Number of vertical layers	$N_l$	72	non-dim
Horizontal Viscosity	$\nu_H$	6.0	$\frac{m^2}{s}$
Diapycnal Viscosity	$\nu_V$	$10^{-3}$	$\frac{m^2}{s}$
Horizontal Diffusivity	$\epsilon_H$	1.0	$\frac{m^2}{s}$
Diapycnal Diffusivity	$\epsilon_V$	$5 \times 10^{-5}$	$\frac{m^2}{s}$
Initial Surface Temperature	$T_t$	-1.9	$^{\circ}C$
Initial Bottom Temperature	$T_b$	1.0	$^{\circ}C$
Initial Surface Salinity	$S_t$	33.8	psu
Initial Bottom Salinity	$S_b$	34.7	psu
Maximum Ocean depth	$H_{ocean}$	720	m
Relaxation Time of Sponge Layer	$T_{sponge}$	0.1	days
Time Step for Static Shelf Experiment	$dt_{Static}$	1000	s
Time Step for Iceberg Calving Experiment	$dt_{Calving}$	10	s

## 8. Supplementary Figures

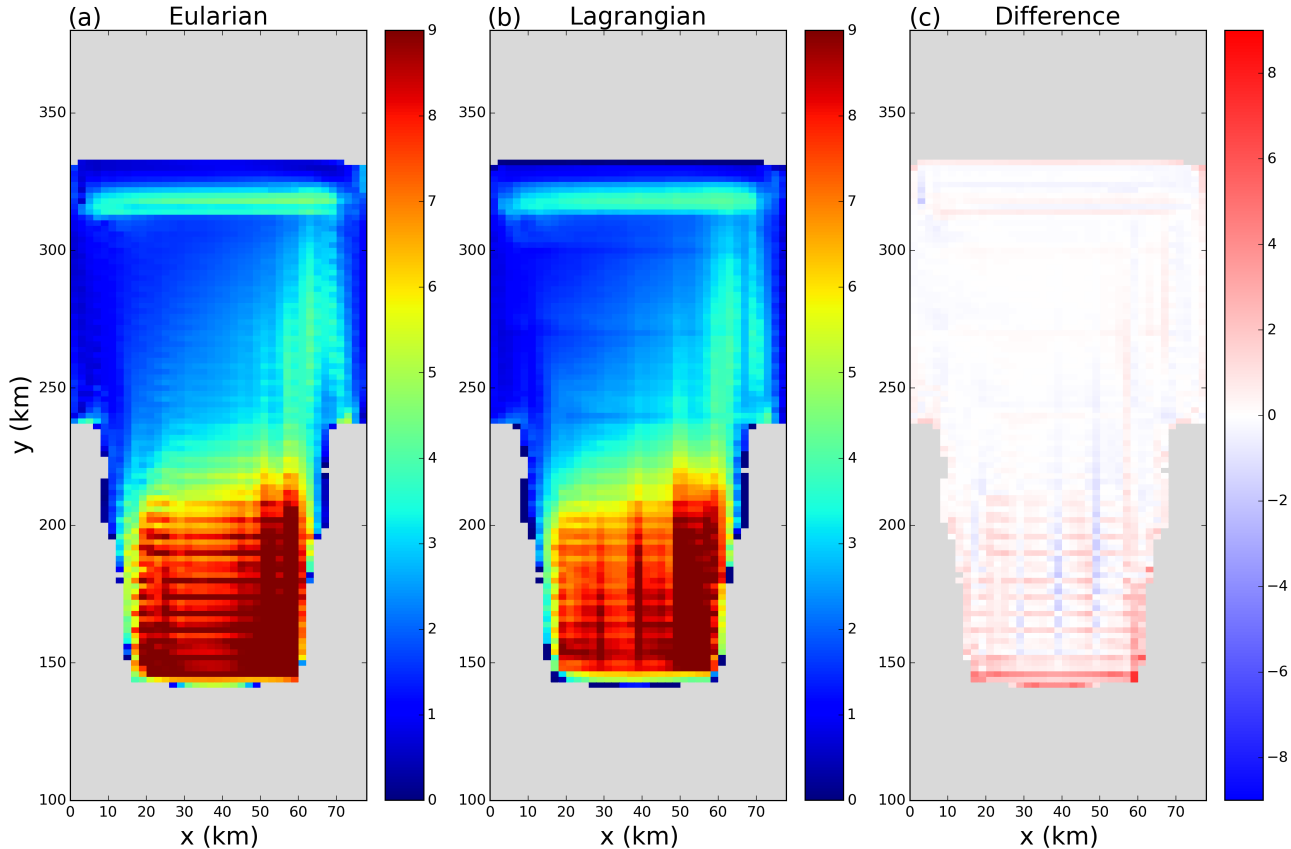


**Figure S1.** Time-averaged melt rates in the (a) Lagrangian and (b) Eulerian simulations in the static ice-shelf configuration. Panel (c) shows the difference between panels (a) and (b). The time averages are taken over 5 years of model time, beginning at the end of the 5 year spin up period.

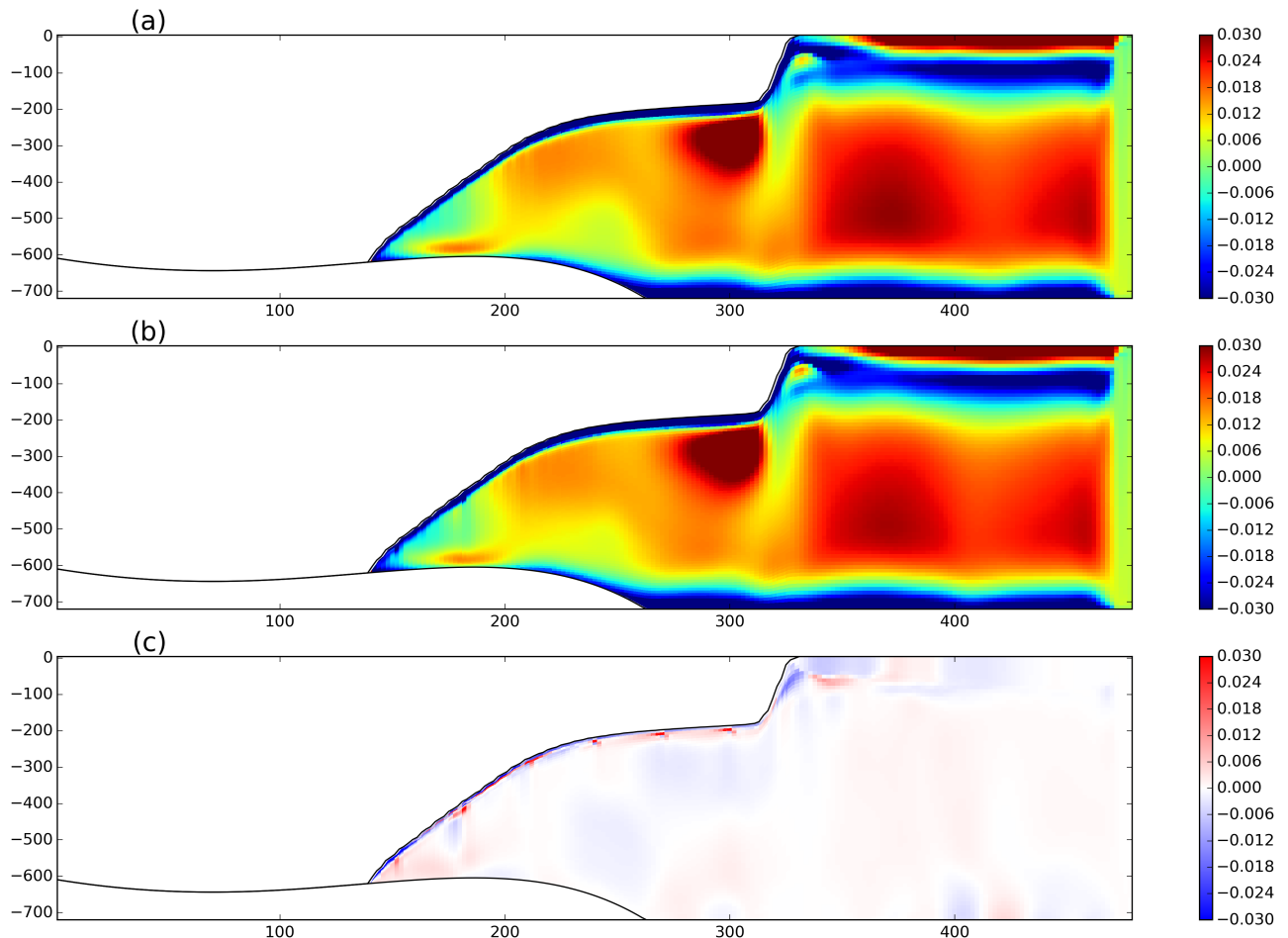


**Figure S2.** Time-averaged vertical sections of salinity in the (a) Lagrangian and (b) Eulerian simulations in the static ice-shelf configuration at  $x=54$  km. Panel (c) shows the difference between panels (a) and (b). The time averages are taken over 5 years of model time, beginning at the end of the 5 year spin up period.

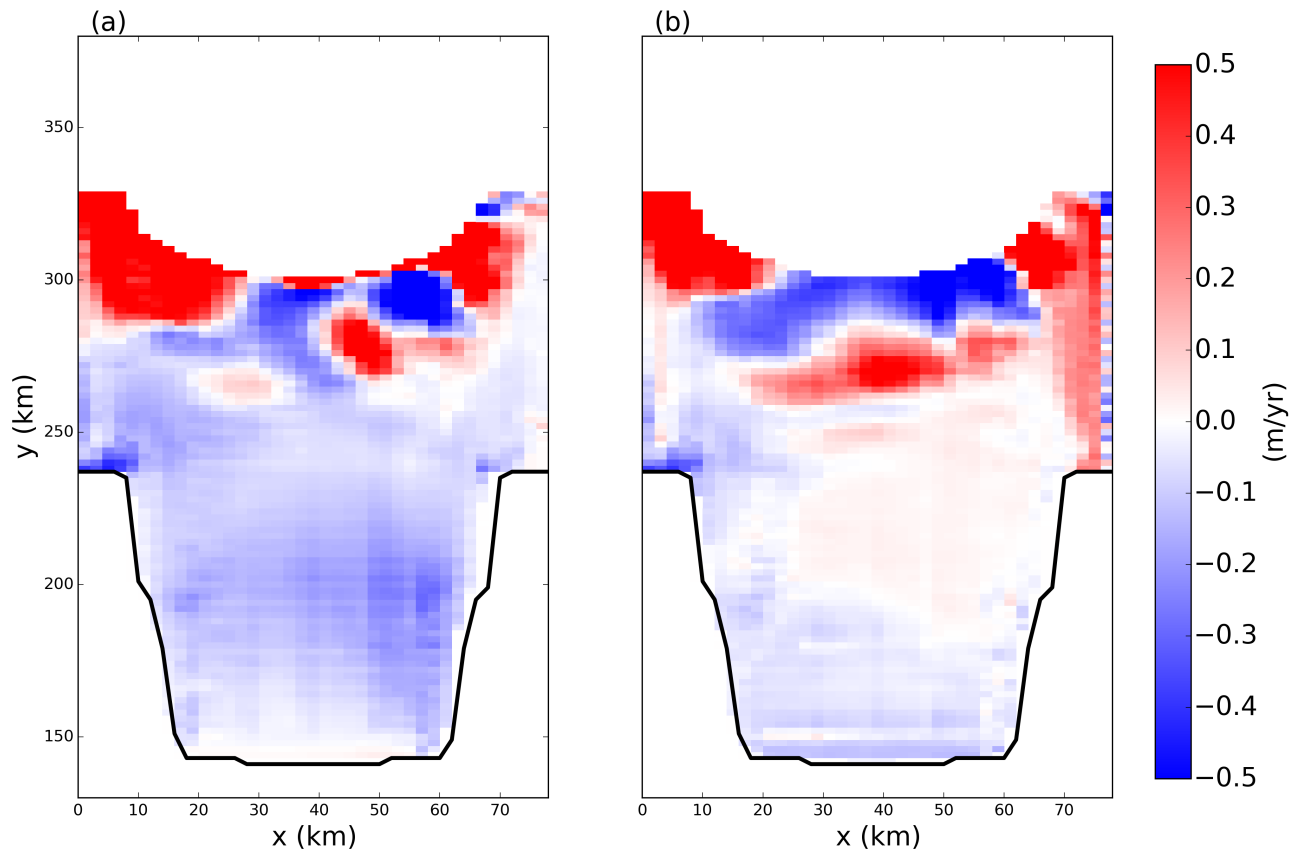


**Figure S3.** (a) Snapshot of the melt rate at the base of the ice shelf 60 days after the calving event in the tabular-iceberg-calving simulation. (b) Steady state melt rate of the simulation that was spun-up from rest with the semi-circular iceberg removed..

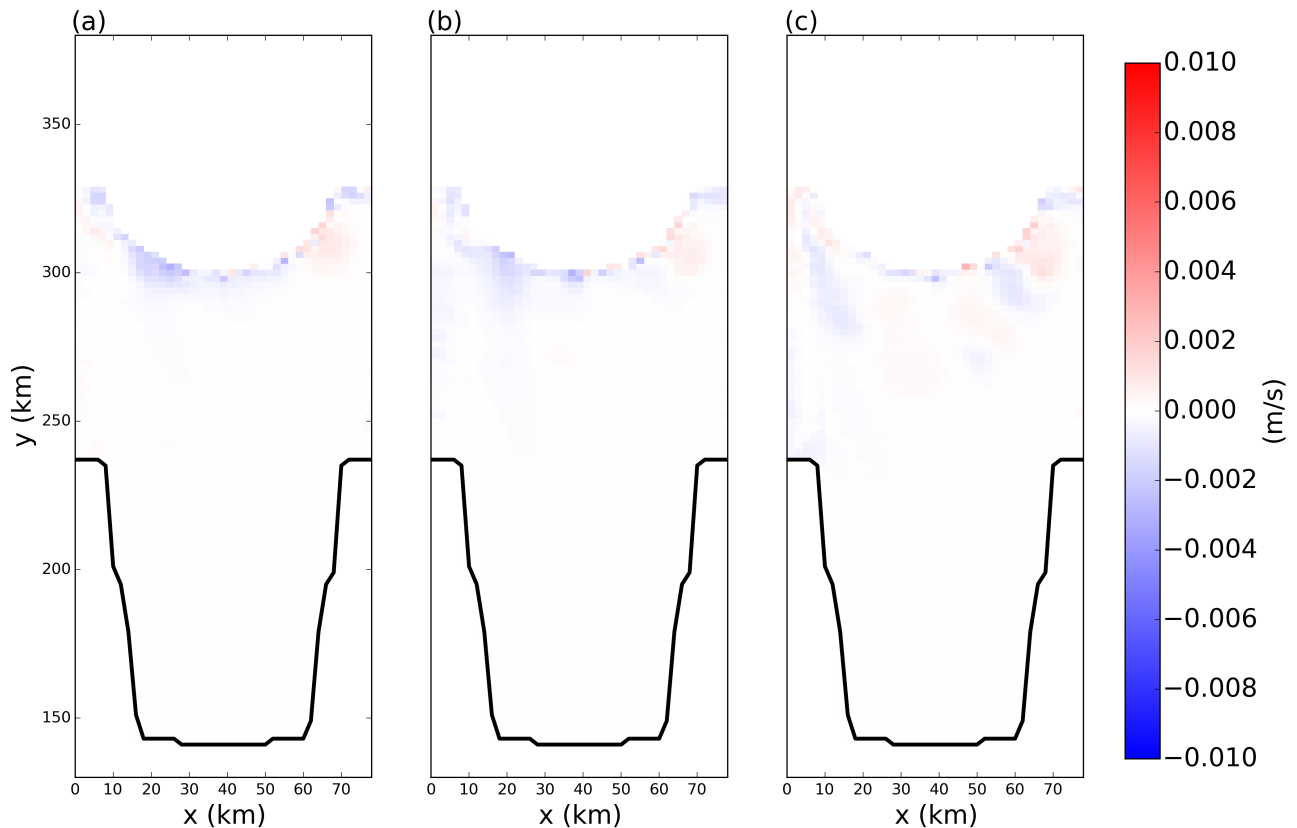


**Figure S4.** Snapshots of frictional velocity at the ice-shelf base in the tabular-iceberg-calving simulation. Snapshots are taken (a) 7, (b) 15, and (c) 50 days after calving.